

# The dynein light chain protein Tda2 functions as a dimerization engine to regulate actin capping protein during endocytosis

Andrew K. Lamb, Andres N. Fernandez, Olve B. Peersen, and Santiago M. Di Pietro\*

Department of Biochemistry and Molecular Biology, Colorado State University, Fort Collins, CO 80523-1870

**ABSTRACT** Clathrin- and actin-mediated endocytosis is a fundamental process in eukaryotic cells. Previously, we discovered Tda2 as a new yeast dynein light chain (DLC) that works with Aim21 to regulate actin assembly during endocytosis. Here we show Tda2 functions as a dimerization engine bringing two Aim21 molecules together using a novel binding surface different than the canonical DLC ligand binding groove. Point mutations on either protein that diminish the Tda2-Aim21 interaction *in vitro* cause the same *in vivo* phenotype as *TDA2* deletion showing reduced actin capping protein (CP) recruitment and increased filamentous actin at endocytic sites. Remarkably, chemically induced dimerization of Aim21 rescues the endocytic phenotype of *TDA2* deletion. We also uncovered a CP interacting motif in Aim21, expanding its function to a fundamental cellular pathway and showing such motif exists outside mammalian cells. Furthermore, specific disruption of this motif causes the same deficit of actin CP recruitment and increased filamentous actin at endocytic sites as *AIM21* deletion. Thus, the data indicate the Tda2-Aim21 complex functions in actin assembly primarily through CP regulation. Collectively, our results provide a mechanistic view of the Tda2-Aim21 complex and its function in actin network regulation at endocytic sites.

## Monitoring Editor

Mary Munson  
University of Massachusetts  
Medical School

Received: Jan 28, 2021

Revised: May 11, 2021

Accepted: May 27, 2021

## INTRODUCTION

Endocytosis is vital for processes such as nutrient uptake, cell signaling, maintenance of membrane composition, and virus internalization. A major endocytic pathway is clathrin-mediated endocytosis (CME), an essential pathway in all eukaryotic cells (McMahon and Boucrot, 2011; Boettner *et al.*, 2012). The CME pathway is highly conserved from yeast to mammalian cells in components, progres-

sion, and function (Merrifield *et al.*, 2002; Newpher *et al.*, 2005; Doyon *et al.*, 2011; Reider and Wendland, 2011; Taylor *et al.*, 2011; Idrissi *et al.*, 2012; Kukulski *et al.*, 2012; Avinoam *et al.*, 2015). CME is a highly choreographed process involving the sequential assembly of nearly 60 proteins at endocytic patches on the plasma membrane (Kaksonen *et al.*, 2005; Taylor *et al.*, 2011; Weinberg and Drubin, 2012). These endocytic factors work together to collect cargo into a clathrin-coated pit, invaginate the surrounding membrane, and pinch off the invagination as a vesicle inside the cell. Despite its crucial role in cell physiology, many aspects of CME and its regulation remain poorly understood. For example, the molecular function of numerous endocytic factors has not been elucidated (Burston *et al.*, 2009; Weinberg and Drubin, 2012; Farrell *et al.*, 2015).

In budding yeast, CME is reliant on polymerization of a branched actin network to provide the force necessary for membrane invagination (Mooren *et al.*, 2012; Goode *et al.*, 2015). When cells are treated with latrunculin A to inhibit actin polymerization, membrane invagination fails to occur and endocytosis is stalled. Numerous regulatory factors are needed for the proper formation of branched actin networks. One key regulator is actin capping protein (CP), which binds to the barbed end of actin filaments with high affinity to prevent the loss or addition of actin subunits (Isenberg *et al.*, 1980;

This article was published online ahead of print in MBoC in Press (<http://www.molbiolcell.org/cgi/doi/10.1091/mbc.E21-01-0032>) on June 3, 2021.

Competing interests: The authors declare no competing financial and nonfinancial interests.

\*Address correspondence to: Santiago M. Di Pietro ([santiago.dipietro@colostate.edu](mailto:santiago.dipietro@colostate.edu)).

Abbreviations used: 3AT, 3-amino-1,2,4-triazole; 5-FOA, 5-fluoroorotic acid; AA, amino acid; BSA, bovine serum albumin; CME, clathrin-mediated endocytosis; CP, capping protein; CPI, capping protein interacting; DLC, dynein light chain; FKBP, FK506 binding protein; GST, glutathione-S-transferase; His-Tda2, 6-histidine-tagged Tda2; MW, molecular weight; PBS, phosphate-buffered saline; PxxP, polyproline motif-rich region; S, sedimentation coefficient; TBR, Tda2 binding region; Y2H, yeast two-hybrid.

© 2021 Lamb *et al.* This article is distributed by The American Society for Cell Biology under license from the author(s). Two months after publication it is available to the public under an Attribution–Noncommercial–Share Alike 3.0 Unported Creative Commons License (<http://creativecommons.org/licenses/by-nc-sa/3.0>).

“ASCB®,” “The American Society for Cell Biology®,” and “Molecular Biology of the Cell®” are registered trademarks of The American Society for Cell Biology.

Kim *et al.*, 2004). CP is a well-conserved heterodimer consisting of an alpha and a beta subunit. Yeast cells with a deletion of the *CAP1* or *CAP2* genes encoding either subunit of CP exhibit an abnormally large actin network and defect in CME (Amatruda *et al.*, 1990; Kaksonen *et al.*, 2005). In higher eukaryotes, regulation of CP by proteins containing a capping protein-interacting (CPI) motif has been demonstrated (Palmgren *et al.*, 2001; Falck *et al.*, 2004; Bruck *et al.*, 2006; Hernandez-Valladares *et al.*, 2010; Edwards *et al.*, 2013, 2014, 2015; Fujiwara *et al.*, 2014; Johnson *et al.*, 2018; Johnston *et al.*, 2018; Hakala, in press). One of the best studied of these is the CARMIL family of proteins, which bind to CP through a CPI motif to regulate the localization and function of CP (Edwards *et al.*, 2014; Stark *et al.*, 2017). While CP is highly conserved throughout eukaryotes, it is unknown whether CPI motifs regulate CP in yeast.

Dynein light chains (DLCs) were first identified as accessory proteins in the microtubule-associated dynein motor complex, where they interact directly with the dynein intermediate chain. However, they have since been reported to interact with a diverse group of proteins and have functions independent of the dynein motor complex (Chuang *et al.*, 2005; Yeh *et al.*, 2006; Conde *et al.*, 2010; Rapali *et al.*, 2011; Clark *et al.*, 2015; Jespersen and Barbar, 2020). Three families of DLCs have been described: the LC8 family, the TcTex1 family, and the roadblock family. All three families form symmetric homodimers with two identical ligand binding sites. While the better-studied LC8 and TcTex1 families share a common fold, the roadblock family has a divergent fold. Interestingly, many of the reported binding partners of DLCs are dimeric or have dimerization domains themselves, including the dynein intermediate chain. Thus, DLCs have been proposed to function as dimerization hubs for their numerous binding partners (Williams *et al.*, 2007; Benison and Barbar, 2009; Hall *et al.*, 2009; Rapali *et al.*, 2011; Jespersen and Barbar, 2020). While yeast has an LC8 DLC that is part of the dynein motor complex, neither TcTex1 nor roadblock were thought to exist until recently.

Tda2 was recently identified as a novel factor in yeast CME (Farrell *et al.*, 2015). The crystal structure of Tda2 demonstrates it to be a symmetric homodimer and, unexpectedly, a structural homolog of the TcTex1 DLC (Farrell *et al.*, 2017). In accord with other DLCs, Tda2 was demonstrated to be a dimer in solution through analytical ultracentrifugation (Farrell *et al.*, 2017). Tda2 does not function as part of the dynein motor complex, but instead forms a complex with the little-studied endocytic factor Aim21, which together localize to CME sites during the actin polymerization stage (Farrell *et al.*, 2017; Shin *et al.*, 2018). Thus, Tda2 represents a unique example of a DLC that works in endocytosis and regulates the actin cytoskeleton. Aim21 (YIR003W) was initially identified in genomewide screenings as a protein localized to CME sites and needed for normal cargo endocytosis as well as for normal mitochondrial inheritance, but how it may accomplish these functions was unclear (Huh *et al.*, 2003; Burston *et al.*, 2009; Hess *et al.*, 2009; Farrell *et al.*, 2015). More recently, a reconstituted Tda2-Aim21 complex was shown to interact with CP *in vitro*, although the significance of this interaction for regulation of actin assembly *in vivo* is a subject of debate (Farrell *et al.*, 2017; Shin *et al.*, 2018). Despite these initial findings on Tda2 and Aim21, how they function at the molecular level during CME remains poorly understood.

Here we uncover the molecular function of Tda2 as a dimerization engine for its binding partner Aim21 and characterize the Tda2-Aim21 complex as an heterotetramer. Tda2-induced dimerization of Aim21 facilitates its proper localization and interaction with CP through a newly defined CPI motif of Aim21. Furthermore, point mutation of the Aim21 CPI motif recapitulates the

endocytic phenotype of *AIM21* gene deletion, suggesting the Tda2-Aim21 complex regulates actin polymerization chiefly through actin CP.

## RESULTS

### The Tda2 binding region of Aim21 maps near its C-terminus and is defined by residues F533 and W536

While it has been established that Aim21 interacts directly with Tda2, the precise region of Aim21 responsible for the interaction is less clear (Farrell *et al.*, 2017; Shin *et al.*, 2018). To determine the region of Aim21 that interacts with Tda2, a series of yeast two-hybrid (Y2H) experiments were performed. Initially, ~100-amino acid (AA) fragments of Aim21 were tested for interaction with Tda2. Of the eight Aim21 fragments tested, only AA 495–595 interacted with Tda2, indicated by growth on selective medium lacking histidine (-HIS; Figure 1A). Growth persisted even at a high concentration of 3-amino-1,2,4-triazole (3AT), indicating a strong interaction (Figure 1A). Stronger growth by the AA 495–595 fragment relative to full-length Aim21 may reflect a higher expression level of the fragment or partial steric hindrance for interaction with full-length Aim21. The AA 495–595 fragment was further sectioned into ~30-AA fragments within the 495–595 region, and interaction with Tda2 was detected for both the AA 510–540 and the AA 525–555 fragments (Supplemental Figure S1). Last, the region spanning AA 510–555 was sectioned into 16-AA fragments. Two overlapping fragments, AA 525–540 and AA 530–545, both displayed an interaction with Tda2 (Figure 1B). The fragments exhibited similar growth even at high concentrations of 3AT, suggesting the AAs shared between the two fragments, AA 530–540, represent the core binding region (Figure 1B).

Having established AA 530–540 as the region of Aim21 that interacts with Tda2, we next wanted to determine which AAs in the region were important for the interaction. A series of glutathione-S-transferase (GST) pull-down assays using purified recombinant proteins were performed to identify the important residues. A truncated Aim21 containing the Tda2 binding region (TBR) was fused to GST (GST-Aim21<sup>510-555</sup>) and alanine scanning mutagenesis was performed between residues 525 and 544. GST-Aim21 fusion proteins were immobilized on glutathione Sepharose resin and subsequently incubated with 6-histidine-tagged Tda2 (His-Tda2). SDS-PAGE analysis showed robust binding of His-Tda2 to GST-Aim21<sup>510-555</sup>, consistent with the Y2H results. Importantly, the W536A mutation abolished the Tda2-Aim21 interaction and the F533A mutant exhibited decreased Tda2 binding (Figure 1C; Supplemental Figure S1B). To further probe the importance of F533 to the Tda2-Aim21 interaction, the experiment was repeated using mutants harboring a second mutation surrounding the F533A mutation. Each of the I530A, E531A, I532A, and N534A mutations significantly exacerbated the Tda2 binding defect seen with F533A alone (Figure 1D; Supplemental Figure S1C). Thus, the Aim21 region spanning AA 530–540 encompasses the TBR, with the large, hydrophobic residues F533 and W536 particularly important for the interaction (Figure 1E). The data also suggest minor contributions to binding from Aim21 residues I530, E531, I532, and N534. Sequence alignment shows the Aim21 TBR is well conserved among fungi, especially key residue W536 (Supplemental Figure S2). There are no clear homologues of Aim21 in higher eukaryotes.

### Tda2 interacts with Aim21 through distinct mechanism from other DLCs

To determine the binding affinity between Tda2 and Aim21, a series of fluorescence polarization assays were performed. A FITC-labeled Aim21 peptide spanning AA 529–539 (FITC-Aim21) was titrated

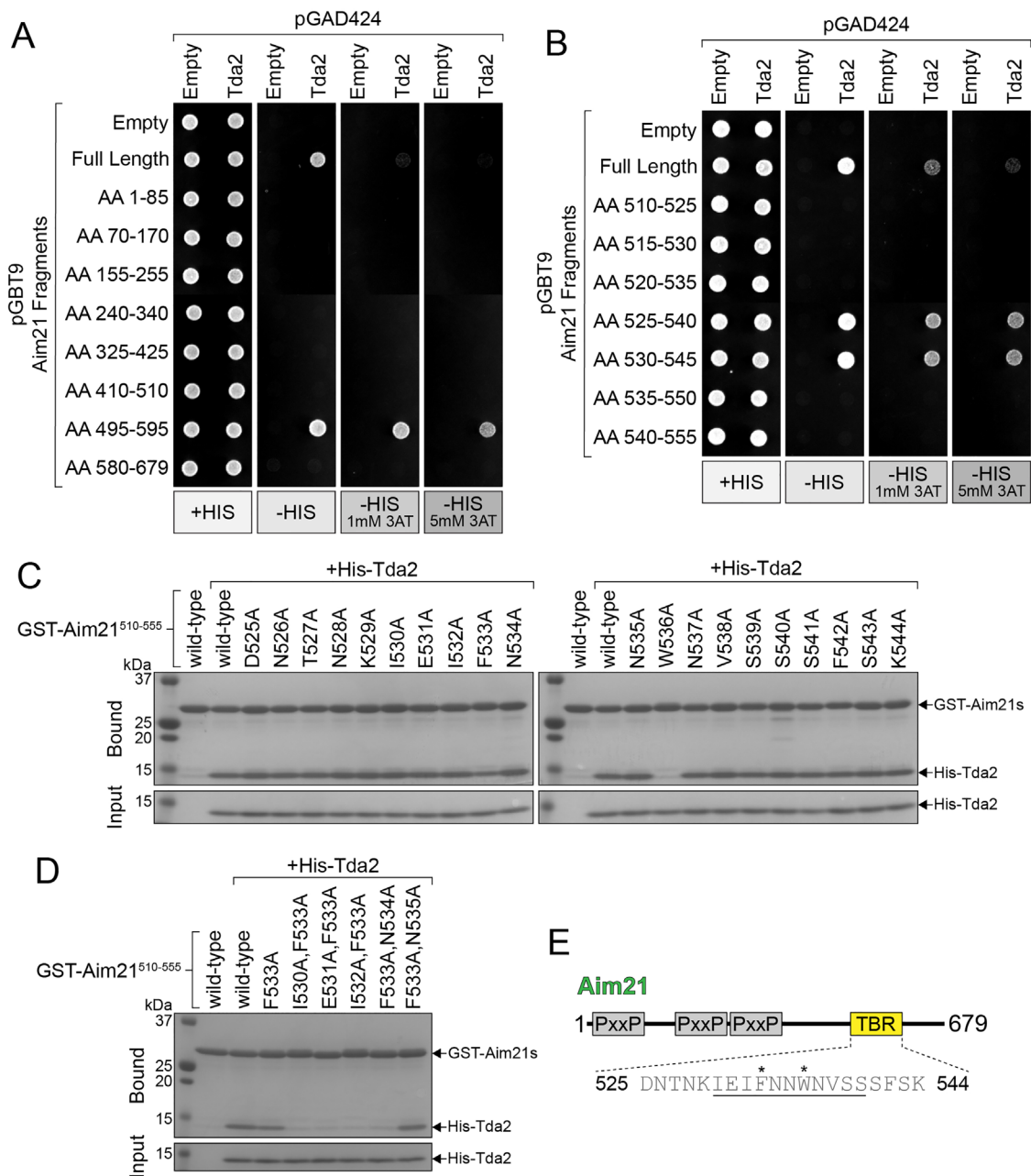


**FIGURE 1:** Tda2 interacts with Aim21 near its C-terminus. (A) Y2H analysis of cells cotransformed with plasmids expressing the GAL4 activation (pGAD424) and binding (pGBT9) domains fused to Tda2 and 100-AA fragments of Aim21, respectively. Cells were spotted onto plates containing histidine (+HIS, control) or selective medium lacking histidine (-HIS) and supplemented with various concentrations of 3AT. Cell growth was detected with full-length Aim21 and AA 495–595 fragment, indicative of an interaction with Tda2. (B) Y2H analysis with Tda2 and varying 16-AA fragments of Aim21 between AA 510–555. Equivalent strength interactions were detected for the AA 525–540 and AA 530–545 fragments. (C) A GST pull-down assay was performed with GST fused to a fragment of Aim21 spanning AA 510–555. The GST-Aim21 fusions either contained no mutations (wild type) or contained a single AA mutated to alanine. Each GST fusion protein was incubated with His-Tda2, and bound proteins were analyzed by SDS–PAGE and Coomassie staining. The W536A mutation to Aim21 severely decreased Tda2 binding, while the F533A mutation showed a moderate decrease. (D) A GST pull-down assay was performed as in C, now using GST-Aim21 fusions with tandem AA mutations. Mutating AAs surrounding F533 exacerbated the effect of the F533A mutation. (E) Organization of Aim21 domains. PxxP, polyproline motif-rich region; The TBR sequence spanning AA 525–540 is shown below Aim21. The underlined sequence spanning AA 530–540 represents the core binding region, and the critical AA F533 and W536 are marked with an asterisk.

with various concentrations of His-Tda2, and fluorescence polarization values were measured. Interestingly, when the data were fit to both one-site and two-site binding isotherms, the bind-

ing was more consistent with the two-site model (Figure 2, A and B, one-site and two-site binding isotherms shown with red and black lines, respectively). Considering the more likely two-site model, the

affinities of the binding events were  $K_{d1}$  of  $1.9 \pm 0.2 \mu\text{M}$  and  $K_{d2}$  of  $28 \pm 3 \mu\text{M}$  (Figure 2B). In comparison, a mutated Aim21 peptide with I532A and F533A (FITC-Aim21\*) exhibited no binding to Tda2, consistent with the GST pull-down data (Figure 2B). To determine the stoichiometry of the higher affinity binding event, a concentration of  $10 \mu\text{M}$  FITC-Aim21, well above  $K_{d1}$ , was titrated with His-Tda2. Binding steadily increased until the concentration reached  $5 \mu\text{M}$  Tda2 dimer and then leveled off, indicative of a 2:1 stoichiometry between Aim21 and the Tda2 homodimer (Figure 2C). These and other data (see below) indicate the high affinity binding event detected by this assay is likely the physiologically relevant binding event and allows a Tda2 homodimer to act as a dimerization engine for Aim21.

Available structures of liganded TcTex1- and LC8-type DLCs show interactions occur in canonical binding grooves where the ligands bind in an extended conformation that effectively adds two strands to the  $\beta$ -sheets found on the two symmetrically equivalent faces of the homodimeric DLCs (Williams et al., 2007). To determine if the Tda2-Aim21 interaction occurs in the same manner, a GST pull-down experiment was performed with Tda2 mutants targeting two distinct regions of the Tda2 homodimer. To disrupt interactions in the canonical  $\beta$ -strand binding groove, residues F86, I103, and K107 of Tda2 were mutated (Figure 2D, top). Additionally, mutations were made to target the top face of the Tda2 homodimer where solvent-exposed hydrophobic pockets could accommodate the largely hydrophobic Aim21 peptide segment residues (Figure 2D, bottom). GST-Aim21<sup>510-555</sup> was immobilized on glutathione Sepharose resin and subsequently incubated with each of the His-Tda2 mutants. SDS-PAGE analysis of bound proteins indicated that the mutations made along the canonical binding groove (F86V, I103Q, and K107E) had little effect on the Tda2-Aim21 interaction (Figure 2E; Supplemental Figure S3A). In contrast, mutations made at the hydrophobic top face (W96H, D101A, D101N, and L124N) had a pronounced decrease in binding (Figure 2E; Supplemental Figure S3A). To confirm the results of the GST pull down in a more quantitative assay, the F86V and D101A mutants were utilized in our fluorescence polarization assay. Consistent with the pull-down results, the F86V mutation had a subtle effect on binding, whereas the D101A mutation displayed little binding to FITC-Aim21 (Figure 2F). Size-exclusion chromatography indicated that neither mutation affected Tda2 homodimer formation (Supplemental Figure S3B). Together, these results suggest that Tda2 interacts with Aim21 at a site different from the canonical binding groove described in other DLCs.

### The Tda2-Aim21 interaction is essential for recruitment and function of Tda2 during CME

Having identified mutations that disrupt the Tda2-Aim21 complex in vitro, we next assessed how these mutations affect the recruitment of each protein to CME sites in vivo. Previously, it was shown that Tda2-GFP was not recruited to endocytic patches in cells carrying a deletion of the *AIM21* gene (*aim21* $\Delta$ ) (Farrell et al., 2017). To test whether disrupting the Tda2-Aim21 interaction had a similar effect, the mutant alleles *aim21*<sup>533,536A</sup> and *tda2*<sup>D101A</sup> were each integrated at their endogenous loci in *TDA2-GFP* cells. Live-cell imaging demonstrated that in both cases, the phenotype matched that of *aim21* $\Delta$  cells, with a total loss in Tda2-GFP and Tda2<sup>D101A</sup>-GFP localization, respectively (Figure 3A). Importantly, immunoblotting of total cell extract showed expression levels of Tda2-GFP and Tda2<sup>D101A</sup>-GFP in mutant strains was comparable to that in control cells (Supplemental Figure S4A). Conversely, recruitment of Aim21-GFP to endocytic sites was shown to be diminished but not abol-

ished in cells carrying a deletion of the *TDA2* gene (*tda2* $\Delta$ ) (Farrell et al., 2017). Here, the mutant alleles *aim21*<sup>533,536A</sup> and *tda2*<sup>D101A</sup> were each integrated at the corresponding endogenous locus in *AIM21-GFP* cells. Live-cell imaging demonstrated the mutations caused a marked reduction of Aim21<sup>533,536A</sup>-GFP and Aim21-GFP recruitment to endocytic sites, respectively (Figure 3B). Quantification of fluorescence intensity at endocytic sites showed such reduction parallels that of Aim21-GFP in *tda2* $\Delta$  cells (Figure 3B, C). Control immunoblotting experiments indicated that expression levels of Aim21<sup>533,536A</sup>-GFP and Aim21-GFP in mutant strains was similar to those of control cells (Supplemental Figure S4B).

As Tda2 was wholly dependent on its interaction with Aim21 for localization to CME sites, we reasoned that cells with a disrupted Tda2-Aim21 interaction would display the same endocytic phenotype as *tda2* $\Delta$  cells. Previously, *tda2* $\Delta$  cells were shown to have a modest reduction in recruitment of actin CP compared with wild-type cells (Farrell et al., 2017). Consistent with this, *aim21*<sup>533,536A</sup> and *tda2*<sup>D101A</sup> cells displayed an equivalent reduction in Cap1-GFP recruitment levels at endocytic sites, as determined by live-cell microscopy (Figure 4, A and B, left). Additionally, the lifetime of Cap1-GFP patches in mutant cells increased slightly compared with wild-type cells (Figure 4B, right). Cells with a defect in CP recruitment show increased levels of the filamentous actin binding protein Abp1 at CME sites. Accordingly, both *tda2* $\Delta$  cells and cells lacking the Tda2-Aim21 interaction showed an appreciable increase in Abp1-GFP levels at endocytic sites (Figure 4, C and D, left). In addition to the increased recruitment, Abp1-GFP patches persisted longer, indicative of a less efficient actin network (Figure 4D, right). Together these in vivo experiments corroborate mapping of the Tda2-Aim21 interaction performed with in vitro assays and indicate Tda2 functions in actin regulation at endocytic sites through its interaction with Aim21.

### Tda2 functions as a dimerization engine for Aim21

DLCs may function as dimerization hubs for their binding partners. Based on the above results, we hypothesized that the Tda2 homodimer may have such a function during yeast CME, helping to bring together two copies of Aim21. To determine if the reconstituted Tda2-Aim21 complex has a size consistent with this hypothesis, we performed size-exclusion chromatography using purified recombinant proteins. His-tagged Aim21, Aim21<sup>533,536A</sup>, and Tda2 were fractionated on a Superose 6 column and the fractions were analyzed by SDS-PAGE. In addition to the purified recombinant proteins, six globular proteins with well-defined hydrodynamic radii were analyzed in parallel. His-Aim21 and His-Aim21<sup>533,536A</sup> had identical elution profiles, both eluting as species larger than the 443 kDa (61 Å) globular standard (Figure 5A). As His-Aim21 has a theoretical molecular weight (MW) of 76.0 kDa, Aim21 is either highly asymmetric, consistent with the prediction that Aim21 is a highly disordered protein, or capable of forming homo-oligomers. The Tda2 homodimer eluted as a much smaller species than Aim21, consistent with its compact structure and MW (Figure 5A). When His-Aim21 and His-Tda2 were combined at equimolar levels, the Tda2-Aim21 complex was successfully reconstituted, indicated by cofractionation of the two proteins (Figure 5A). Notably, the elution volume indicated the hydrodynamic radius of the complex was larger than that of the 669 kDa (86 Å) standard (Figure 5A). The sizeable shift in elution volumes between Tda2-Aim21 and Aim21 could not be explained by the addition of a 31 kDa Tda2 homodimer to Aim21 alone, supporting the idea that Tda2 links multiple copies of Aim21. His-Aim21<sup>533,536A</sup> showed no cofractionation with His-Tda2 on incubation of the two proteins,

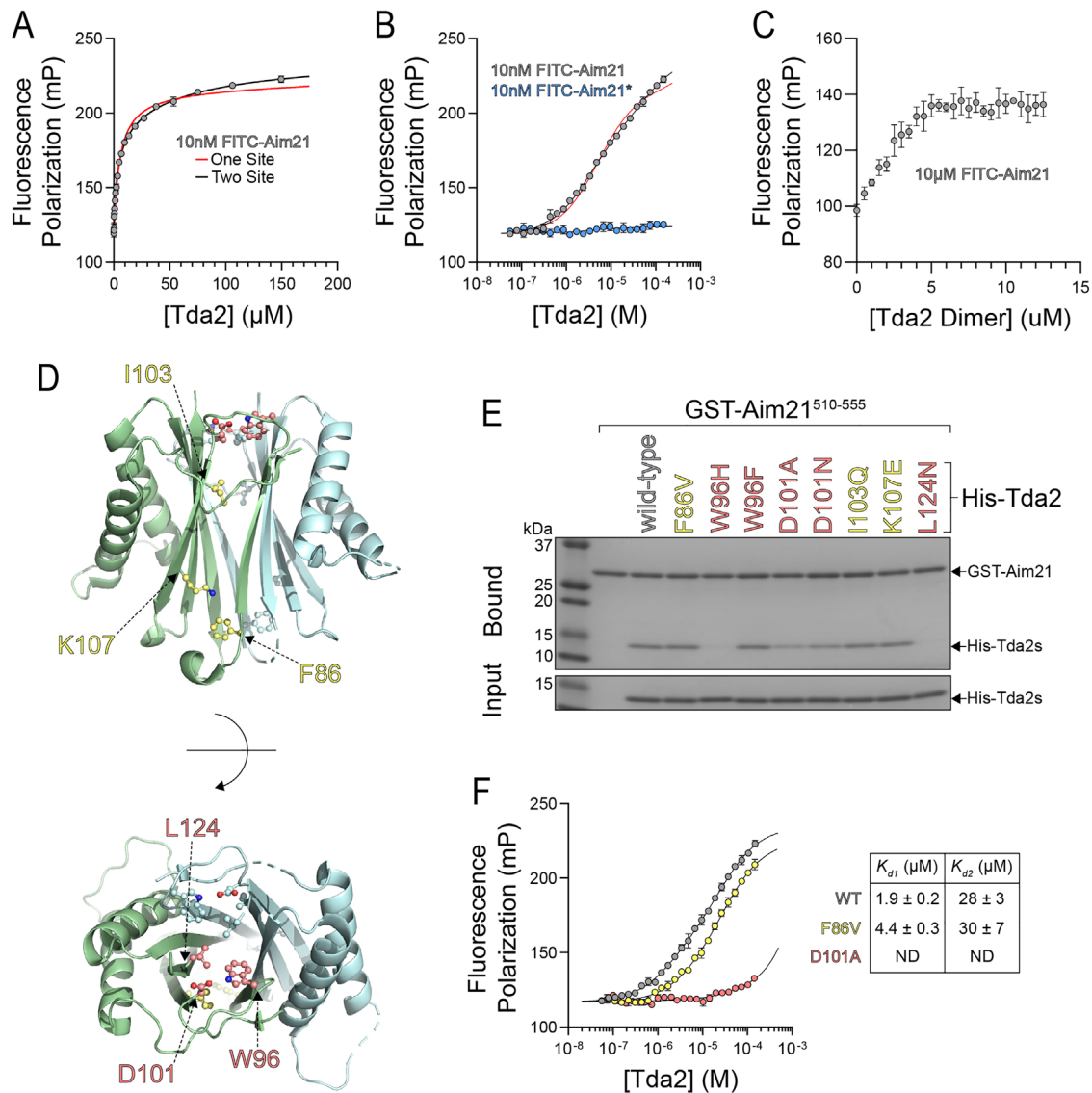


**FIGURE 2:** Tda2 interacts with Aim21 through distinct mechanism. (A) A fluorescence polarization assay was performed using 10 nM FITC-labeled Aim21 peptide spanning AA 529–539 (FITC-Aim21) and various concentrations of His-Tda2. Data points represent the average and SD from a single representative experiment performed in three technical replicates. Note that error is too small for most Tda2 concentration data points to produce an error bar larger than the symbol. The data were fit to both 1-site (red line) and 2-site (black line) binding isotherms. The Tda2-Aim21 interaction most likely occurs through a 2-site model. (B) A fluorescence polarization assay was performed using either 10 nM FITC-Aim21 peptide (FITC-Aim21; KIEIFNNWNVS) or a mutant peptide (FITC-Aim21\*; KIEAANNWNVS). FITC-Aim21\* displayed no interaction with Tda2. The data were fit to both 1-site (red line) and 2-site (black line) binding isotherms. (C) A fluorescence polarization assay was performed using 10  $\mu\text{M}$  FITC-Aim21 peptide and various concentrations of His-Tda2. FITC-Aim21 became saturated at a Tda2 dimer concentration of 5  $\mu\text{M}$ , indicating a stoichiometry of 2:1 between Aim21 and the Tda2 dimer for the high affinity binding event. (D, top) Crystal structure of the Tda2 homodimer (PDB entry 5VKY). One Tda2 molecule is shown in pale green and the other in pale cyan. The residues F86, I103, and K107 are colored yellow and indicated with arrows on one Tda2 molecule. These residues sit along the canonical  $\beta$ -strand binding groove that has been described for other DLC–ligand interactions. (Bottom) The Tda2 homodimer is rotated 90° for a view of the top face of the homodimer. The residues W96, D101, and L124 are shown as spheres and colored in salmon and indicated with arrows on one Tda2 molecule. (E) GST pull-down assay data from GST fused to a fragment spanning AA 510–555 of Aim21. Each GST fusion protein was incubated with either His-Tda2 (wild type) or His-Tda2 containing a single AA mutation. Bound proteins were analyzed by Coomassie staining. Mutating AA W96, D101, and L124 of Tda2 resulted in a significant decrease in interaction with Aim21, while mutating AA F86, I103 and K107 had little or no effect. (F) A fluorescence polarization assay was performed using 10 nM FITC-Aim21 and various concentrations of His-Tda2 (WT) or Tda2 mutants (F86V and D101A). Data points represent the average and SD from a single experiment performed in triplicate. Dissociation constants represent the mean  $\pm$  SEM of data from three independent experiments each fit to a two-site binding isotherm. ND, not determined.

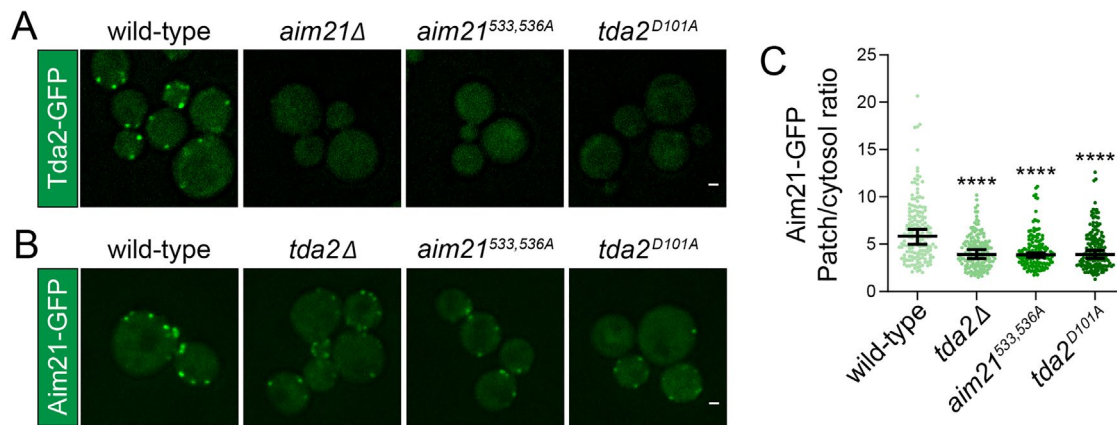


**FIGURE 3:** Recruitment of Tda2 and Aim21 to endocytic sites is dependent on their interaction. (A) Live-cell fluorescence microscopy showing no recruitment to endocytic sites of Tda2-GFP expressed from the endogenous locus in cells lacking Aim21 (SDY1291) or cells with a disrupted Tda2-Aim21 interaction (SDY1297 and SDY1466). Scale bar, 1  $\mu$ m. (B) Live-cell fluorescence microscopy showing reduced recruitment to endocytic sites of Aim21-GFP expressed from the endogenous locus in cells lacking Tda2 (SDY1290) or cells with a disrupted Tda2-Aim21 interaction (SDY1324 and SDY1467). Scale bar, 1  $\mu$ m. (C) Quantification of Aim21-GFP fluorescence intensity at endocytic patches in wild type, *tda2* $\Delta$ , *aim21*<sup>533,536A</sup>, and *tda2*<sup>D101A</sup> cells. From left to right, median patch/cytosol ratio = 5.85, 3.90, 3.87, and 3.90 and  $n = 161, 162, 155,$  and  $164$ . Error bars, median with 95% CI. \*\*\*\* $P \leq 0.0001$ .

confirming that the mutations abolish the Tda2-Aim21 interaction (Figure 5A).

These initial findings suggested Tda2 and Aim21 interact to form an asymmetric, elongated complex. To corroborate this, the proteins were fractionated in a 5–20% (wt/vol) sucrose gradient to separate samples based on density. Four globular standard proteins with known sedimentation coefficients (S) were analyzed in parallel. His-Aim21 and His-Aim21<sup>533,536A</sup> were concentrated in fractions 4 and 5, displaying a similar density to the 43 kDa (3.6 S) standard (Figure 5B). Tda2 eluted primarily in fractions 3 and 4, consistent with its MW and fold (Figure 5B). When Aim21 and Tda2 were combined to reconstitute the Tda2-Aim21 complex, the proteins cofractionated in fractions 6 and 7, and the complex displayed a similar density to the 66 kDa (4.6 S) standard (Figure 5B).

Analysis of the size-exclusion chromatography and sucrose gradient fractionation data suggests the Tda2 homodimer interacts with two Aim21 molecules, resulting in a four-subunit complex. From our fractionation experiments, Stokes radii and S were estimated for Tda2, Aim21, and the Tda2-Aim21 complex, allowing us to calculate an experimental MW for each species. Tda2 displayed an experimental MW of  $24.9 \pm 0.4$  kDa ( $27.2 \pm 0.3$  Å and  $2.3 \pm 0.1$  S), similar to the 31.1 kDa theoretical MW of the homodimer. Aim21 displayed an experimental MW of  $94.6 \pm 5.6$  kDa ( $79.5 \pm 2.2$  Å and  $2.9 \pm 0.1$  S), in line with the 76.0 kDa theoretical MW of an Aim21 monomer. Last, the experimental MW of the Tda2-Aim21 complex was  $206.5 \pm 7.9$  kDa ( $108.4 \pm 0.9$  Å and  $4.7 \pm 0.1$  S). This MW compares nicely with the 183.0 kDa theoretical MW of a complex consisting of one Tda2 homodimer and two Aim21 molecules.

To further test if Tda2 could function as a dimerization factor for Aim21, a GST pull-down assay was performed to assess if GST-fused Aim21 could interact with supplemental Aim21. GST-Aim21 was first immobilized on glutathione resin, then incubated with His-tagged Aim21 (His-Aim21 or His-Aim21<sup>533,536A</sup>). GST-Aim21 did not pull down His-Aim21 when Tda2 was not present (Figure 5C, lane 2). When GST-Aim21 was incubated with both His-Tda2 and His-Aim21, the supplemental Aim21 was now pulled down (Figure 5C, lane 3). When His-Aim21<sup>533,536A</sup> was used in place of wild-type His-Aim21, it was no longer pulled down by GST-Aim21 despite the presence of

His-Tda2 (Figure 5C, lane 4). The data are consistent with the idea that formation of the Tda2-Aim21 complex is reliant on the ability of two Aim21 molecules to interact directly with the Tda2 homodimer, thus supporting the proposed function of Tda2 as a dimerization engine for Aim21.

### Chemical dimerization of Aim21 rescues the *tda2* $\Delta$ endocytic phenotype

Previously, we demonstrated *tda2* $\Delta$  cells have a phenotype characterized by decreased recruitment of Aim21 and increased levels of Abp1, indicative of an overgrown actin network at CME sites (Figures 3 and 4). As our in vitro data support Tda2 acting as a dimerization engine for Aim21, we reasoned that artificial dimerization of Aim21 could rescue the *tda2* $\Delta$  phenotype.

To test this, we utilized a chemically induced dimerization system consisting of FK506 binding protein (FKBP) and the bivalent chemical AP20187, which induces homodimerization of FKBP (Clackson *et al.*, 1998; Neff and Blau, 2001; Mionnet *et al.*, 2008; Kolos *et al.*, 2018). Yeast strains were engineered to express Abp1-mCherry and full-length Aim21 tagged with both FKBP and GFP (Aim21<sup>FL</sup>-FKBP-GFP) from their endogenous loci. Incorporation of the FKBP tag did not affect Aim21-GFP expression or patch dynamics, as Aim21-GFP and Aim21<sup>FL</sup>-FKBP-GFP were expressed at comparable levels and displayed equivalent patch lifetimes (Supplemental Figure S5, A and B). In cells with functional Tda2 (*TDA2*), treatment with AP20187 did not affect recruitment of Aim21<sup>FL</sup>-FKBP-GFP when compared with the vehicle (EtOH) control (Figure 6, A, top, and B). Additionally, Abp1-mCherry levels at CME sites were indistinguishable between the AP20187 and EtOH groups (Figure 6, A, top, and C). As expected, *tda2* $\Delta$  cells showed diminished Aim21<sup>FL</sup>-FKBP-GFP recruitment and increased Abp1-mCherry levels with vehicle alone (Figure 6, A, middle, B, and C). Interestingly, on incubation with AP20187, *tda2* $\Delta$  cells displayed a marked increase in Aim21<sup>FL</sup>-FKBP-GFP recruitment (Figure 6, A, middle, and B). While chemical dimerization of Aim21 resulted in nearly a full rescue of its recruitment to endocytic sites, rescue of the Abp1-mCherry level at endocytic sites was partial (Figure 6, A, middle, and C). Strikingly, cells expressing Aim21<sup>1-535</sup>-FKBP-GFP, with the dimerizing element placed at the

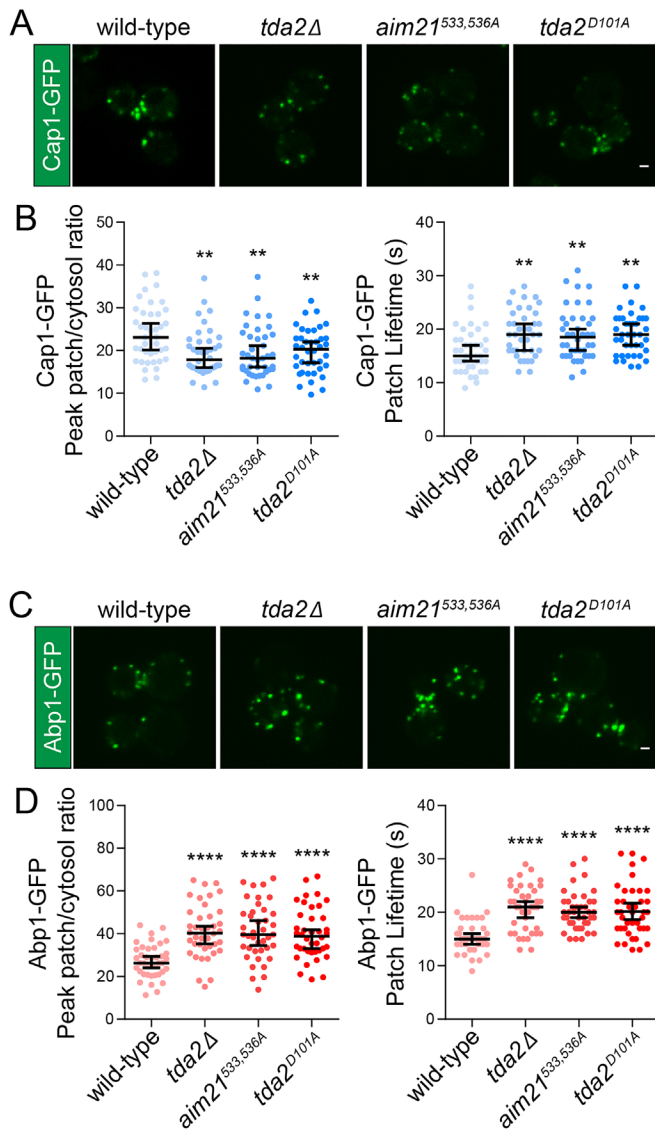


**FIGURE 4:** Disruption of the Tda2-Aim21 interaction mimics the *tda2Δ* endocytic phenotype. (A) Live-cell fluorescence microscopy showing reduced levels of Cap1-GFP at endocytic sites in cells lacking Tda2 (SDY1293) or cells with a disrupted Tda2-Aim21 interaction (SDY1298 and SDY1468). Scale bar, 1  $\mu$ m. (B, left) Quantification of Cap1-GFP peak fluorescence intensity at endocytic patches in wild type, *tda2Δ*, *aim21*<sup>533,536A</sup>, and *tda2*<sup>D101A</sup> cells. From left to right, median peak patch/cytosol ratio = 23.1, 17.9, 18.2, and 20.3 and  $n = 40$  for all groups. (Right) Quantification of Cap1-GFP patch lifetime at endocytic patches in wild type, *tda2Δ*, *aim21*<sup>533,536A</sup>, and *tda2*<sup>D101A</sup> cells. From left to right, median patch lifetime = 15.0, 19.0, 18.5, and 19.0 and  $n = 40$  for all groups. Error bars, median with 95% CI. **\*\*** $P \leq 0.01$ . (C) Live-cell fluorescence microscopy showing increased levels of Abp1-GFP at endocytic sites in cells lacking Tda2 (SDY1295) or cells with a disrupted Tda2-Aim21 interaction (SDY1299 and SDY1469). Scale bar, 1  $\mu$ m. (D, left) Quantification of Abp1-GFP peak fluorescence intensity at endocytic patches in wild type, *tda2Δ*, *aim21*<sup>533,536A</sup>, and *tda2*<sup>D101A</sup> cells. From left to right, median peak patch/cytosol ratio = 26.3, 40.3, 39.6, and 38.9 and  $n = 40$  for all groups. (Right) Quantification of Abp1-GFP patch lifetime at endocytic patches in wild type, *tda2Δ*, *aim21*<sup>533,536A</sup>, and *tda2*<sup>D101A</sup> cells. From left to right, median patch lifetime = 15.0, 21.0, 20.0, and 20.0 and  $n = 40$  for all groups. Error bars, median with 95% CI. **\*\*\*\*** $P \leq 0.0001$ .

TBR of a C-terminal truncated Aim21, exhibited a full rescue of the phenotype on AP20187 treatment, with both Aim21<sup>1-535</sup>-FKBP-GFP and Abp1-mCherry recruitment levels comparable to wild-type cells (Figure 6, A, bottom, B, and C). Examining the patch lifetime of Abp1-mCherry showed the same trend, with cells expressing Aim21<sup>1-535</sup>-FKBP-GFP displaying a more complete rescue than Aim21<sup>FL</sup>-FKBP-GFP expressing cells on FKBP dimerization (Figure 6D). Together, these findings suggest that Tda2 functions as a dimerization engine for Aim21 in vivo, which is necessary for normal actin polymerization during endocytosis.

### Aim21 contains a CP interacting motif

Given the direct physical interaction of the Tda2-Aim21 complex with CP (Farrell et al., 2017), we reasoned that Tda2 or Aim21 may contain a CPI motif that facilitates the interaction. When we analyzed the primary AA sequence of Aim21 against the consensus CPI motif sequence (Bruck et al., 2006; Hernandez-Valladares et al., 2010), two potential CPI motifs were identified. To test whether either of these regions were responsible for the interaction with CP, a GST pull-down experiment was performed with GST fused to wild-type Aim21 or Aim21 harboring point mutations to the potential CPI motif. In each mutant, three closely positioned basic residues, which are prevalent in CPI motifs, were mutated to glutamic acid. GST-Aim21 and the mutants (GST-Aim21<sup>504,507,509E</sup> and GST-Aim21<sup>564,566,573E</sup>) were immobilized on glutathione resin and subsequently incubated with His-Tda2 and His-Cap1/2. While both mutants showed interaction with Tda2, GST-Aim21<sup>504,507,509E</sup> displayed no interaction with CP, suggesting the mutated region contained a CPI motif (Figure 7A). Notably, the region containing the potential CPI motif in Aim21, spanning AA 495–515, lies directly adjacent to the TBR (Figure 7B).

We next wanted to test if the potential CPI motif of Aim21 was functionally relevant in vivo. Previously, we reported that recruitment of the Tda2-Aim21 complex to the actin network at endocytic sites depends at least in part on Aim21 interaction with Bbc1 (Farrell et al., 2017). Furthermore, while deletion of *TDA2* or *AIM21* resulted in lower levels of CP at sites of endocytosis, deletion of *CAP1* caused higher levels of Tda2-Aim21 complex at endocytic sites, suggesting the Tda2-Aim21 complex helps recruit CP rather than the converse model (Farrell et al., 2017). Interestingly, when mutations to disrupt the Aim21 CPI motif were integrated into the genome of *AIM21-GFP* cells (*aim21*<sup>504,507,509E</sup>-*GFP*), Aim21 displayed a different recruitment phenotype compared with cells unable to form the Tda2-Aim21 complex (*aim21*<sup>533,536A</sup>-*GFP*, Figure 7C). While Aim21<sup>533,536A</sup>-GFP had a deficit in recruitment to endocytic sites, Aim21<sup>504,507,509E</sup>-GFP had a significant increase in recruitment (Figure 7, C, top, and D). This is probably due to a larger than normal actin network in *aim21*<sup>504,507,509E</sup> cells (see below). Importantly, this difference was not due to a change in expression levels between Aim21-GFP, Aim21<sup>533,536A</sup>-GFP, and Aim21<sup>504,507,509E</sup>-GFP (Supplemental Figure S6). Most importantly and consistent with the idea that Aim21 residues 495–515 define a CPI motif, *aim21*<sup>504,507,509E</sup> cells showed a deficit in Cap1-GFP recruitment to sites of endocytosis (Figure 7, C, middle, and E). The defect in Cap1-GFP recruitment was more pronounced in *aim21*<sup>504,507,509E</sup> cells than in *aim21*<sup>533,536A</sup>, with *aim21*<sup>504,507,509E</sup> cells exhibiting a similar defect to those lacking Aim21 (*aim21Δ*, Figure 7, C, middle, and E). Last, Abp1-GFP levels were significantly elevated in *aim21*<sup>504,507,509E</sup> cells, consistent with an overgrown actin network at CME sites (Figure 7, C bottom, and F). Together, these results suggest the CPI motif identified in Aim21 is important for regulation of CP localization and function at CME

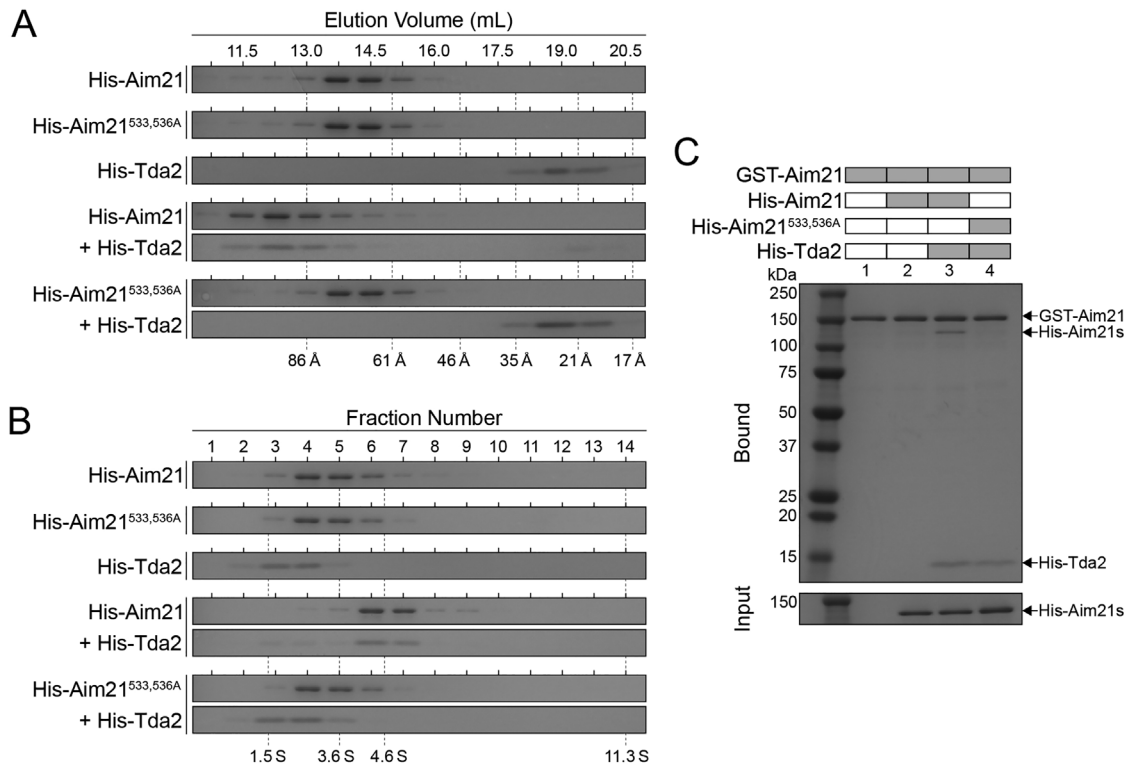


**FIGURE 5:** Tda2 functions as a dimerization engine for Aim21. (A) Purified recombinant His-Aim21 and His-Aim21<sup>533,536A</sup> were incubated with buffer alone or His-Tda2 and fractionated by size-exclusion chromatography on a Superose 6 column. Fractions were analyzed by SDS-PAGE. Stokes radii of six standard proteins are shown at the bottom. The reconstituted Tda2-Aim21 complex runs as a much larger complex than Aim21 alone. (B) Purified recombinant His-Aim21 and His-Aim21<sup>533,536A</sup> were incubated with buffer alone or His-Tda2 and fractionated in a 5–20% (wt/vol) linear sucrose gradient. Fractions were analyzed by SDS-PAGE. Sedimentation coefficients of four standard proteins are shown at the bottom. The reconstituted Tda2-Aim21 complex runs as a slightly larger complex than Aim21 alone. (C) A GST pull-down assay was performed with GST fused to Aim21. GST fusion proteins were incubated with His-Aim21 alone (lane 2), His-Aim21 and His-Tda2 (lane 3), or His-Aim21<sup>533,536A</sup> and His-Tda2 (lane 4). Bound proteins were analyzed by SDS-PAGE and Coomassie staining. GST-Aim21 only displayed an interaction with His-Aim21 in the presence of His-Tda2.

sites. Moreover, the fact that the Abp1-GFP phenotype is not more severe in *aim21Δ* cells than in *aim21<sup>504,507,509E</sup>* cells suggests the negative regulation of Aim21 on actin assembly at endocytic sites is mostly dependent on its interaction with CP.

#### Dimerization of Aim21 near CPI motif facilitates interaction with actin CP

Having determined the CPI motif of Aim21 facilitates interaction of the Tda2-Aim21 complex with CP, we next wanted to examine the interaction of Aim21 with CP in a more quantitative manner. To determine the binding affinity between Aim21 and CP, a fluorescence polarization assay was performed. A FITC-labeled Aim21 peptide containing both the CPI motif and TBR of Aim21 (FITC-Aim21<sup>CPI+TBR</sup>) was titrated with various concentrations of CP, and fluorescence polarization values were measured. The data were fit to a one-site binding model, yielding a  $K_d$  value of  $3.1 \pm 0.2 \mu\text{M}$  (Figure 8A). To determine the effect of reconstitution of the Tda2-Aim21 complex on the binding affinity, the experiment was repeated in the presence of 25  $\mu\text{M}$  His-Tda2. Strikingly, the  $K_d$  value of the binding event decreased to  $250 \pm 13 \text{ nM}$ , representing a ~12-fold increase in binding affinity (Figure 8A). These data are consistent with previous findings from pull-down experiments and together support the idea that Tda2 is necessary for the efficient interaction between Aim21 and CP.

Given the potential function of Tda2 as a dimerization engine for Aim21, we hypothesized that artificial dimerization of Aim21 could replicate the ability of the reconstituted Tda2-Aim21 complex to bind CP. To test this, we exploited the dimeric nature of the glutathione S-transferase tag in a GST pull-down assay using purified recombinant proteins. As GST is a strong parallel dimer, and its interaction with glutathione does not occur when in monomeric form, all GST fusion protein bound to glutathione resin will be dimeric fusion proteins. Accordingly, Aim21 was tagged with GST either at its N- or at its C-terminus, immobilized on glutathione Sepharose resin, and incubated with 6-histidine-tagged CP (His-Cap1/2 heterodimer). While the reconstituted Tda2-Aim21 complex displayed a robust interaction with CP, GST-Aim21 alone, dimerized by GST at its N-terminus, was not able to interact efficiently with CP (Figure 8, B, lanes 1 and 2, and C). When the GST tag was flipped to the C-terminus of Aim21, Aim21 showed a modest interaction with CP, even in the absence of Tda2 (Figure 8, B, lane 3, and C). Notably, as Aim21 was truncated and the C-terminal GST tag was moved closer to the TBR of Aim21 (AA 530–540), the degree of CP binding increased, showing optimal levels when the GST tag was placed at AA 535 (Figure 8, B, lanes 4 and 5, and C). Thus, dimerization of Aim21 at its C-terminus appears to facilitate the efficient interaction between Aim21 and CP, and this dimerization is most effective when located close to the CPI motif as it happens naturally for the TBR of

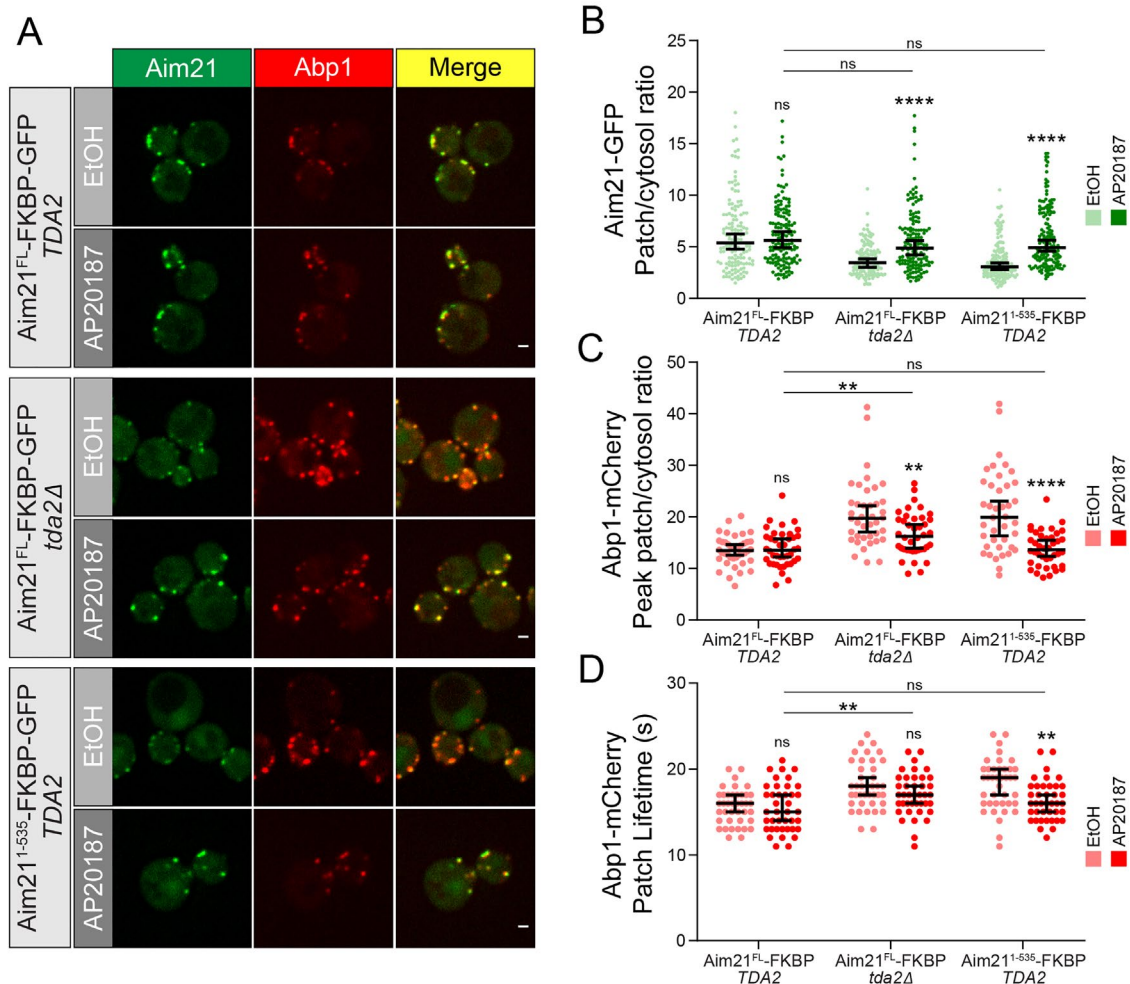


**FIGURE 6:** Chemically induced dimerization of Aim21 rescues the phenotype of *tda2Δ* cells. (A) Yeast strains were created to express Abp1-mCherry and Aim21 tagged with both FKBP and GFP (Aim21<sup>FL</sup>-FKBP-GFP or Aim21<sup>1-535</sup>-FKBP-GFP) from their endogenous loci. Prior to imaging, cells were incubated with EtOH (vehicle) or AP20187 (FKBP dimerizer). (Top) Live-cell fluorescence microscopy of cells expressing Aim21<sup>FL</sup>-FKBP-GFP and Tda2 (SDY1378) showing no change in levels of Aim21<sup>FL</sup>-FKBP-GFP and Abp1-mCherry on treatment with AP20187. (Middle) Cells expressing Aim21<sup>FL</sup>-FKBP-GFP but lacking Tda2 (SDY1378) display an increase in Aim21<sup>FL</sup>-FKBP-GFP and a decrease in Abp1-mCherry patch intensity levels on treatment with AP20187. (Bottom) Cells expressing Aim21<sup>1-535</sup>-FKBP-GFP and Tda2 (SDY1431) display an increase in Aim21<sup>1-535</sup>-FKBP-GFP and a decrease in Abp1-mCherry patch intensity on treatment with AP20187. Note the similarities between AP20187 groups in the three panels. Scale bars, 1  $\mu$ m. (B) Quantification of Aim21<sup>FL</sup>-FKBP-GFP and Aim21<sup>1-535</sup>-FKBP-GFP fluorescence intensity at endocytic patches showing chemical dimerization of Aim21 can rescue the defect in Aim21 recruitment seen in cells lacking a Tda2-Aim21 complex. From left to right, median patch/cytosol ratio = 5.36, 5.61, 3.46, 4.98, 3.07, and 4.91 and  $n = 138, 146, 131, 146, 141,$  and  $158$ . Error bars, median with 95% CI; ns  $P > 0.05$ , \*\*\*\* $P \leq 0.0001$ . (C) Quantification of Abp1-mCherry peak fluorescence intensity at endocytic patches showing chemical dimerization of Aim21 can rescue the increased levels of Abp1 recruitment seen in cells lacking a Tda2-Aim21 complex. From left to right, median peak patch/cytosol ratio = 13.5, 13.5, 19.7, 16.2, 20.0, and 13.6 and  $n = 40$  for all groups. Error bars, median with 95% CI; ns  $P > 0.05$ , \*\* $P \leq 0.01$ , \*\*\*\* $P \leq 0.0001$ . (D) Quantification of Abp1-mCherry patch lifetime showing chemical dimerization of Aim21 can rescue the increased Abp1 patch lifetime seen in cells lacking a Tda2-Aim21 complex. From left to right, median patch lifetime = 16.0, 15.0, 18.0, 17.0, 19.0, and 16.0 and  $n = 40$  for all groups. Error bars, median with 95% CI; ns  $P > 0.05$ , \*\* $P \leq 0.01$ .

Aim21. Alternatively, it is possible that the position of the GST tag in the fusion protein may affect accessibility of the CPI motif to interact with CP.

## DISCUSSION

The function of DLCs has been a subject of debate. Similarly, the molecular function of Tda2, the recently discovered *Saccharomyces cerevisiae* TcTex1 DLC, is poorly understood. Unveiling the function of Tda2 would not only establish its role in yeast CME

but also provide insight into the function of DLCs in other eukaryotes. Here we reveal that the Tda2 homodimer functions as a dimerization engine for Aim21 during CME. Tda2-induced dimerization of Aim21 in turn facilitates its localization and interaction with CP through a newly defined CPI motif in Aim21. The finding of a CPI motif in yeast suggests a conserved mechanism of CP regulation outside mammalian cells and the fact that it operates in endocytosis implies a broader function than previously appreciated (Edwards *et al.*, 2014).

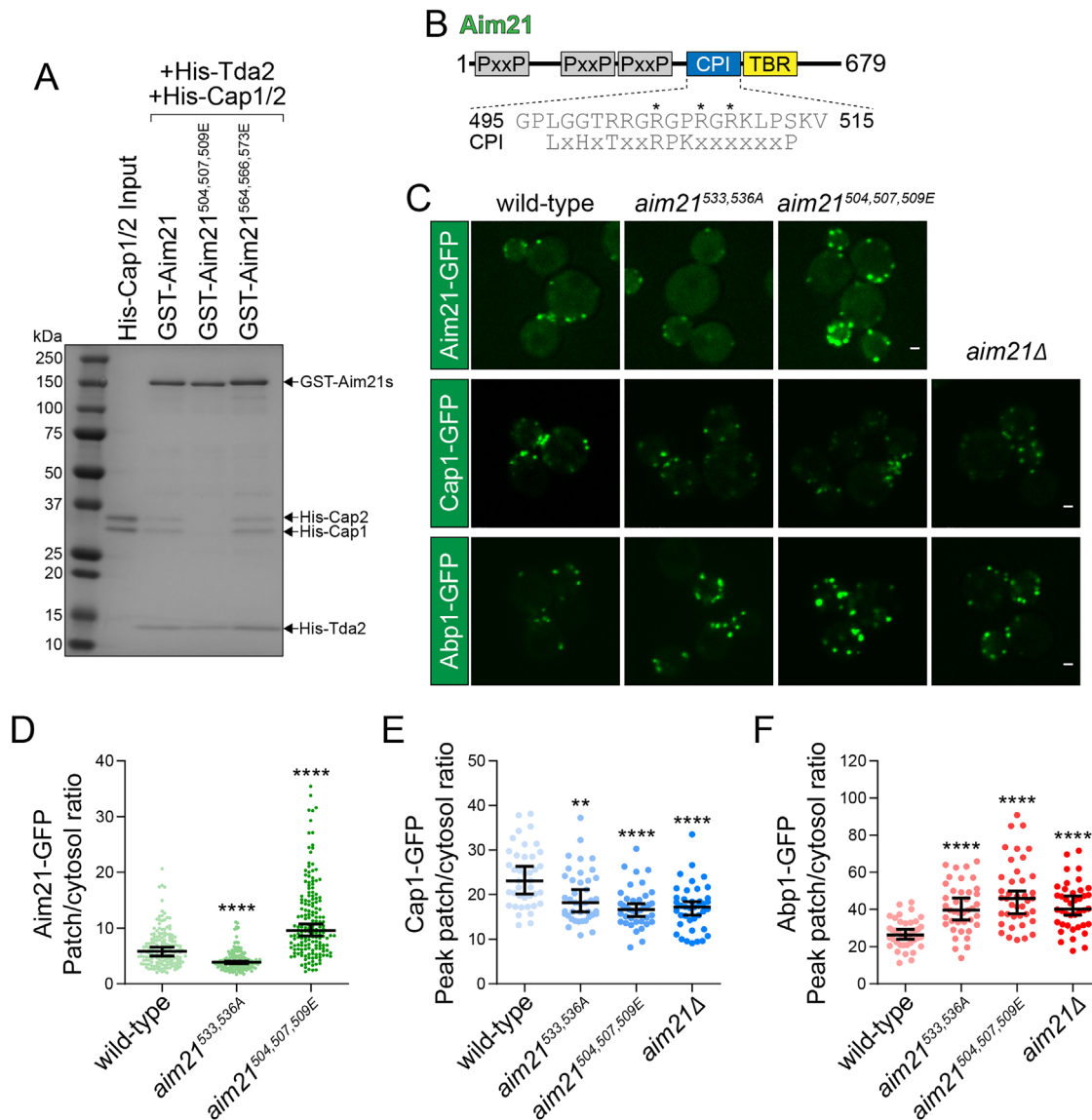


**FIGURE 7:** Aim21 contains a CPI motif. (A) A GST pull-down assay was performed with GST fused to Aim21. The GST-Aim21 fusions either contained no mutations or contained three basic residues mutated to glutamic acid in potential CPI motifs of Aim21 (GST-Aim21<sup>504,507,509E</sup> and GST-Aim21<sup>564,566,573E</sup>). Each GST fusion protein was incubated with His-Tda2 and His-Cap1/2, and bound proteins were analyzed by SDS-PAGE and Coomassie staining. The GST-Aim21<sup>504,507,509E</sup> mutant displayed a significant decrease in binding with His-Cap1/2 compared with GST-Aim21 or GST-Aim21<sup>564,566,573E</sup>. (B) Organization of Aim21 domains. PxxP, polyproline motif-rich region. The CPI motif sequence spanning AA 495–515 is shown below Aim21, with residues that were mutated to disrupt the Aim21-CP interaction denoted with an asterisk. The consensus CPI motif sequence that has been described previously is shown for comparison. (C, top) Live-cell fluorescence microscopy showing reduced recruitment of Aim21-GFP to endocytic sites in cells with a disrupted Tda2-Aim21 interaction (SDY1324). In contrast, cells lacking the Aim21-CP interaction (SDY1472) display an increase in Aim21-GFP patch intensity. (Bottom) Live-cell fluorescence microscopy showing decreased recruitment of Cap1-GFP and increased recruitment of Abp1-GFP to endocytic sites in cells lacking the Aim21-Tda2 interaction (SDY1298 and SDY1299), the Aim21-CP interaction (SDY1474 and SDY1434), and Aim21 (SDY1292 and SDY1294). Scale bars, 1  $\mu$ m. (D) Quantification of Aim21-GFP fluorescence intensity at endocytic patches in wild type, *aim21*<sup>533,536A</sup>, and *aim21*<sup>504,507,509E</sup> cells. From left to right, median patch/cytosol ratio = 5.85, 3.87, and 9.58 and  $n = 161$ , 155, and 170. Error bars, median with 95% CI. \*\*\*\* $P \leq 0.0001$ . (E) Quantification of Cap1-GFP peak fluorescence intensity at endocytic patches in wild type, *aim21*<sup>533,536A</sup>, *aim21*<sup>504,507,509E</sup>, and *aim21Δ* cells. From left to right, median peak patch/cytosol ratio = 23.1, 18.2, 16.6, and 17.2 and  $n = 40$  for all groups. Error bars, median with 95% CI. \*\* $P \leq 0.01$ , \*\*\*\* $P \leq 0.0001$ . (F) Quantification of Abp1-GFP peak fluorescence intensity at endocytic patches in wild type, *aim21*<sup>533,536A</sup>, *aim21*<sup>504,507,509E</sup>, and *aim21Δ* cells. From left to right, median peak patch/cytosol ratio = 26.3, 39.6, 46.0, and 40.2 and  $n = 40$  for all groups. Error bars, median with 95% CI. \*\*\*\* $P \leq 0.0001$ .

DLCs have been suggested to function as hub proteins that induce dimerization of their numerous interacting partners (Williams *et al.*, 2007; Benison and Barbar, 2009; Hall *et al.*, 2009; Rapali *et al.*, 2011; Jespersen and Barbar, 2020). Given this, we proposed a model in which Tda2 functions to bind to and induce dimerization of two Aim21 subunits. A number of our findings are in support of this model: 1) biochemistry indicates Aim21 itself is a monomer and thus is capable of being dimerized. 2) Fluorescence polarization and GST pull-down assays confirmed the Tda2 homodimer has the ability to bind two Aim21 subunits. 3) The experimental MW of the reconstituted Tda2-Aim21 complex was in agreement with the theoretical MW of a complex consisting of one Tda2 homodimer and two Aim21 molecules. 4) The endocytic phenotype of *tda2Δ* cells was rescued by chemically induced dimerization of Aim21. Given that Tda2 is wholly dependent on its interaction with Aim21 for recruitment to endocytic sites, its role in dimerization and thus regulation of Aim21 may be the sole function it has in CME. Numerous proteins that interact with DLCs are also reported to contain domains capable of dimerization, such as coiled coils (Williams *et al.*, 2007; Benison and Barbar, 2009; Hall *et al.*, 2009; Rapali *et al.*, 2011). Accordingly, we previously hypothesized that Tda2 could be inducing dimerization of Aim21 through a predicted coiled coil near the N-terminus of Aim21 (residues 82–110). However, gel filtration and density gradient fractionation experiments indicated that this predicted coiled coil does not mediate Aim21 dimerization and was unimportant for the formation and of the Tda2-Aim21 complex (Supplemental Figure S7). While we cannot rule out that such a dimerizing element exists in Aim21, our study did not indicate that such a region was necessary.

The interaction between DLCs and their binding partners has largely been shown to occur through extension of the DLC  $\beta$ -sheet using symmetric binding grooves on opposite sides of the DLC dimers (Williams *et al.*, 2007). However, recent evidence has suggested that some TcTex1 members may have a noncanonical binding site in addition to the canonical binding groove, potentially allowing for formation of ternary complexes (Merino-Gracia *et al.*, 2015). When analyzing the structure of Tda2, the canonical binding groove is partly occupied by the N-terminus of Tda2, which is extended in *S. cerevisiae* compared with the structures of TcTex1 from higher eukaryotes, suggesting an interaction between Tda2 and Aim21 in a canonical manner is hindered (Williams *et al.*, 2005, 2007; Farrell *et al.*, 2017). In line with this, mutations to a hydrophobic pocket away from the canonical binding groove greatly affected the Tda2-Aim21 interaction, while mutations along the canonical binding groove had little effect. This suggests that the canonical binding mode for TcTex1 interactions is not conserved from yeast to mammals. Previously, DLCs associated with the dynein motor complex have been proposed to function as cargo adaptors, with one binding site interacting with cargo and the other with the dynein-intermediated chain. However, thermodynamic arguments oppose this function as the already dimeric DLCs would likely favor a dimeric binding partner (Williams *et al.*, 2007; Hall *et al.*, 2009). If a second binding site similar to the hydrophobic site of Tda2 were present in other TcTex1 DLCs, a cargo adaptor function would be plausible.

Is the Tda2-Aim21 complex constitutively assembled or dynamically assembled and disassembled *in vivo*? We previously performed gel filtration fractionation analysis of wild-type yeast cytosol and observed two peaks for Tda2 (Farrell *et al.*, 2017). The first peak corresponds to a cohort of Tda2 in complex with Aim21 and the second peak to the Tda2 homodimer. Deficiency of one subunit of a constitutively associated protein complex often results in destabi-

lization of the other complex subunits. In contrast, we observed that deletion of *TDA2* did not destabilize Aim21 and, conversely, deletion of *AIM21* did not destabilize Tda2 as determined by immunoblotting of total cell extracts (Farrell *et al.*, 2017) (see also Supplemental Figure S4). These results suggest Tda2-Aim21 may not necessarily form a constitutively associated complex. Further work will be needed to test this possibility and to elucidate any mechanism potentially regulating complex assembly/disassembly.

Our data suggest dimerization of Aim21 is not only critical for its proper localization during CME but also critical for its function. However, dimerization is only part of the equation, as dimerization of Aim21 specifically at the TBR appears to be necessary for the full function of Aim21. While chemically induced dimerization of Aim21 at its C-terminus partially rescued the Abp1 defect in *tda2Δ* cells, dimerization at the TBR of Aim21 resulted in a full rescue. Similarly, artificial dimerization of Aim21 at its C-terminus allowed for a weak interaction with CP *in vitro*, whereas artificial dimerization at residue 535 resulted in a stronger interaction. How could dimerization of Aim21 be facilitating an efficient interaction with CP? First, it could be through an avidity effect. Given the proximity of the TBR and CPI motif, dimerization of Aim21 would put two CPI motifs nearby, resulting in a bivalent ligand for CP. When CP dissociates from one of the Aim21 binding sites, the nearby binding site could subsequently rebind CP, limiting its diffusion, and resulting in an increased functional affinity. This possibility is supported by the increased affinity of CP for FITC-Aim21<sup>CPI+TBR</sup> in the presence of Tda2. Second, auto-inhibition of Aim21 could prevent the Aim21-CP interaction, with Tda2-induced dimerization relieving the inhibition. This mechanism would require the Tda2-Aim21 interaction to be regulated in the same way. Last, Tda2 dimerization of Aim21 could lead to formation of secondary structure, which may be necessary for the Aim21-CP interaction. Opposing this idea, CPI motifs from higher eukaryotes are believed to be disordered in the absence of CP, and the CPI segment binds to the CP complex in an extended conformation that does not have any regular secondary structure. Regardless of the method, the idea that the CP-CPI motif interaction can be altered through allosteric regulation of the CPI motif had not previously been shown.

In mammalian cells, regulation of CP by a family of proteins containing CPI motifs has been demonstrated (Edwards *et al.*, 2014). In addition to allosterically regulating the affinity of CP for the barbed end of actin filaments, some CPI motif-containing proteins have been shown to aid in localization of CP (Edwards *et al.*, 2015). Given the relative simplicity of the yeast actin network, it was previously unknown whether CPI motifs were present in yeast. Our discovery of a functional CPI motif in Aim21 supports the notion that the binding of CP to actin filaments is a regulated event in yeast. Further supporting this idea, Twinfilin, a protein involved in CME and conserved from yeast to humans, interacts with CP and was recently shown to contain a CPI motif in mice (Palmgren *et al.*, 2001; Falck *et al.*, 2004; Johnston *et al.*, 2018). Given the experimentally tractable yeast endocytic actin network, the study of these CPI motif containing proteins in *S. cerevisiae* could help shed light on remaining questions about CP regulation. For instance, how Twinfilin regulates CP is a subject of debate, with one report proposing mammalian Twinfilin has a procapping function, while other studies provide evidence for an uncapping function (Johnston *et al.*, 2018; Hakala *et al.*, 2021; Mwangangi *et al.*, 2021). However, the function of Twinfilin is complex as, at least *in vitro*, it can directly regulate filament barbed-end dynamics independent of CP and either increase or decrease depolymerization rate depending on the nucleotide state of the barbed-end actin subunits (ADP-P<sub>i</sub> vs. ADP) (Shekhar *et al.*, 2021).

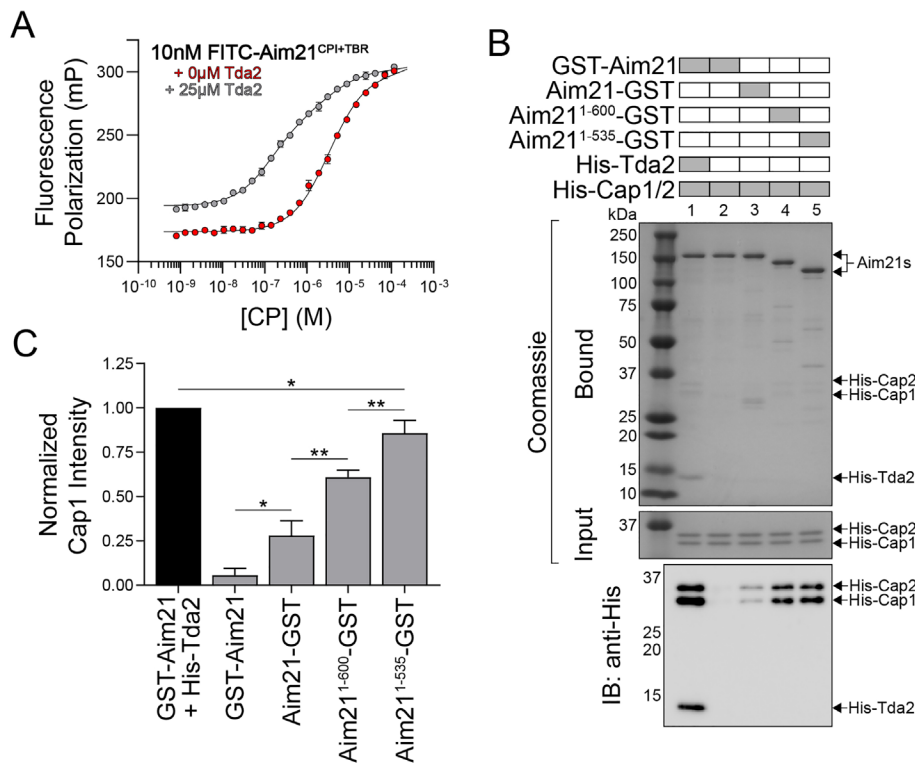


**FIGURE 8:** Dimerization of Aim21 near CPI motif facilitates interaction with actin CP. (A) A fluorescence polarization assay was performed using 10 nM FITC-labeled Aim21 peptide spanning AA 493–539 (FITC-Aim21<sup>CPI+TBR</sup>) and various concentrations of His-Cap1/2 (CP). Reactions either included 25 μM His-Tda2 or lacked His-Tda2 (0 μM). Data points represent the average and SD from a single experiment performed in three technical replicates. Note that error is too small for many CP concentration data points to produce an error bar larger than the symbol. Dissociation constants represent the mean ± SEM of data from three independent experiments fit to a one-site binding isotherm. (B) A GST pull-down assay was performed with GST-Aim21 (lanes 1 and 2), Aim21-GST (lane 3), Aim21<sup>1-600</sup>-GST (lane 4), and Aim21<sup>1-535</sup>-GST (lane 5). GST fusion proteins were incubated with either His-Cap1/2 alone (lanes 2, 3, 4, and 5) or His-Cap1/2 and His-Tda2 (lane 1). Bound proteins were analyzed by SDS-PAGE and Coomassie staining (top) and anti-His immunoblotting (bottom). Dimerization of Aim21 at its C-terminus by GST allowed for interaction with His-Cap1/2 at comparable levels to the reconstituted Tda2/Aim21 complex. (C) Quantification of normalized His-Cap1 intensity from GST pull down in B;  $n =$  three independent experiments. Error bars, mean with SD. \* $P \leq 0.05$ , \*\* $P \leq 0.01$ .

Additionally, our data with the Aim21 CPI motif mutant showing a decreased CP levels at endocytic sites support the idea that Aim21 aids in recruitment of CP to the actin network at CME sites, similar to the role of CARMIL in higher eukaryotes at other cellular membranes (Edwards *et al.*, 2015). Interestingly, besides regulation of CP to CME sites, Aim21 may also have a direct effect inhibiting actin filament barbed-end elongation (Shin *et al.*, 2018). However, the fact that the increased Abp1-GFP levels at endocytic sites are not higher in *aim21Δ* cells compared with *aim21<sup>504,507,509E</sup>* cells suggests the main mechanism for Aim21 capping of actin filament barbed end is through CP. While our data support that the CPI motif of Aim21 is critical for its function and contributes to CP recruitment to sites of endocytosis, more work will be needed to fully understand how exactly it is regulating CP.

In conclusion, we have uncovered the molecular function of Tda2 as a dimerization engine for Aim21 during CME in *S. cerevisiae*. Formation of the Tda2-Aim21 complex is essential for its interaction with and regulation of CP, supporting the idea that regulation of CP through CPI motifs is conserved from yeast to humans.

## MATERIALS AND METHODS

[Request a protocol](#) through *Bio-protocol*.

### Plasmids and yeast strains

All cloning was performed using the In-fusion HD Cloning System (Takara Bio). Plasmids for Y2H analysis of Aim21 fragments were generated by PCR amplification of the corresponding DNA fragments of AIM21 and cloned into pGBT9. Generation of pGAD424-Tda2 was described previously (Farrell *et al.*, 2017). Generation of plasmids for bacterial expression of recombinant GST-Aim21 and His-Tda2 was described previously (Farrell *et al.*, 2017). The plasmid for expression of recombinant GST-Aim21<sup>510-555</sup> was generated by PCR amplification of the corresponding AIM21 DNA sequence and cloned into pGEX-5X-1. The plasmids for expression of recombinant His-Aim21, His-Cap1 and His-Cap2 were generated by PCR amplification of the corresponding DNA sequences of AIM21, CAP1, and CAP2 and cloned into pET30a(+). Plasmids for expression of recombinant Aim21 tagged at the C-terminus with GST (Aim21-GST) were generated by amplification of the GST encoding sequence from pGEX-5X-1 and cloned into pET30a(+)-AIM21, resulting in an N-terminal 6-histidine-tagged and a C-terminal GST-tagged protein. For fair comparison in this experiment, a 6-histidine tag was cloned into pGEX-5X-1-Aim21 at its C-terminus. All plasmids encoding mutant recombinant proteins were engineered by PCR-based mutagenesis using the In-fusion system. All constructs were verified by DNA sequencing.

For plasmids designed to integrate mutations into the *S. cerevisiae* genome, fragments containing the full ORF of either AIM21 or TDA2 plus 100 base pairs upstream and downstream were generated by

PCR amplification from yeast genomic DNA and cloned into pUC18. PCR-based mutagenesis of pUC18-AIM21 and pUC18-TDA2 yielded the template for genetic manipulation. Plasmids for FKBP integration into the yeast genome were generated by PCR amplification of the DNA sequence encoding Aim21-GFP from the corresponding yeast GFP library strain (Invitrogen), then cloned into pUC18. Subsequently, the FKBP encoding sequence was amplified from a gene block and cloned into pUC18-AIM21-GFP between the Aim21 and the GFP encoding sequences.

The background *S. cerevisiae* strain BY4741 (*MATa*, *his3Δ1*, *leu2Δ0*, *met15Δ0*, *ura3Δ0*) was used throughout this study. Wild-type GFP-expressing strains (Tda2-GFP, Aim21-GFP, Cap1-GFP, and Abp1-GFP) were obtained from the yeast GFP library (Invitrogen). Integration of mutant alleles was performed using a two-step gene replacement approach described previously (Di Pietro *et al.*, 2010). As an example, SDY1297 (*MATa*, *his3Δ1*, *leu2Δ0*, *met15Δ0*, *ura3Δ0*, *TDA2-GFP::HIS3*, *aim21<sup>533,536A</sup>*) was created from the Tda2-GFP library strain (*MATa*, *his3Δ1*, *leu2Δ0*, *met15Δ0*, *ura3Δ0*, *TDA2-GFP::HIS3*). In step one, URA3 was amplified from pRS316

(Sikorski and Hieter, 1989) using primers that impart 50 base pairs of homology to the sequences directly upstream and downstream of the *AIM21* ORF, then transformed (Ito *et al.*, 1983) into the Tda2-GFP library strain to generate intermediate strain SDY1291 (*MATa*, *his3Δ1*, *leu2Δ0*, *met15Δ0*, *ura3Δ0*, *TDA2-GFP::HIS3*, *aim21Δ::URA3*). Second, the intermediate strain SDY1291 was transformed with a DNA fragment containing the mutant allele *aim21<sup>533,536A</sup>*. Cells were grown overnight on plates containing rich media, then replica was plated onto plates containing 5-fluoroorotic acid (5-FOA). Colonies that grew on plates containing 5-FOA represented cells in which the *aim21<sup>533,536A</sup>* allele replaced *URA3*. For FKBP strains used in the chemical-induced dimerization experiment, BY4741 cells were first subjected to mCherry tagging of the *ABP1* ORF by PCR amplification of pFA6a-mCherry-HIS3MX6 and homologous recombination, followed by markerless integration of *AIM21-FKBP-GFP* fragments using the two-step approach described. All integrants were verified by PCR of genomic DNA. All yeast strains generated in this study are listed in Supplemental Table S1.

## Y2H assay

AH109 cells were cotransformed with pGBT9 and pGAD424 vectors (Takara Bio) and grown on synthetic dropout media lacking leucine and tryptophan. Successful cotransformants were grown overnight in synthetic dropout media lacking leucine and tryptophan. The following day, cells were diluted to an O.D. 600 of 0.2 in sterile water. Diluted cells were spotted on synthetic dropout media lacking leucine and tryptophan (control), or lacking histidine in addition; 3AT was used to test for increased binding stringency.

## Biochemical methods

Recombinant 6-histidine (His) and GST fusion proteins were expressed in BL21 codon plus *Escherichia coli* and purified using His-Pur Cobalt Resin (Thermo Scientific) or glutathione Sepharose 4 Fast Flow (GE Healthcare) as previously described (Feliciano and Di Pietro, 2012). Recombinant Aim21 proteins tagged with both His and GST at either terminus were first purified using glutathione Sepharose 4 Fast Flow and subsequently purified using HisPur Cobalt Resin. All proteins were dialyzed in phosphate-buffered saline (PBS; 137 mM NaCl, 2.7 mM KCl, 10 mM Na<sub>2</sub>HPO<sub>4</sub>, 2 mM KH<sub>2</sub>PO<sub>4</sub>).

GST pull-down assays were performed as previously described (Bultema *et al.*, 2014). In short, recombinant GST-tagged proteins (10 μg) were incubated with glutathione Sepharose resin for 30 min at 4°C. Equimolar His-tagged protein was added and incubated for an additional 30 min. Resin was washed 3× in PBS containing Triton X-100 (0.1–0.5%) and boiled in Laemmli sample buffer. Bound proteins were analyzed by SDS-PAGE and Coomassie staining and/or immunoblotting with anti-6xHis (Sigma). All pull downs were repeated in an independent experiment to ensure reproducibility and in three independent experiments if quantification was included. For quantification of pull-down experiments, ImageJ software was used for determining the intensity of protein bands. His-tagged protein band intensities were first normalized to the intensity of the immobilized GST protein and next to the wild-type condition, depicted as a black bar in the figures. Statistical significance between groups was determined using an unpaired Student's *t* test (GraphPad Prism Software).

Fluorescence polarization assays were performed as previously described (Feliciano *et al.*, 2015). Briefly, 10 nM of FITC-labeled Aim21 peptide was titrated with various concentrations of His-Tda2, His-Tda2 mutants, and His-Cap1/2 in experiment buffer (137 mM NaCl, 2.7 mM KCl, 10 mM Na<sub>2</sub>HPO<sub>4</sub>, 2 mM KH<sub>2</sub>PO<sub>4</sub>, 0.01% Triton X-100, 2 mM DTT). For the stoichiometry experiment (Figure 2C),

10 μM FITC-Aim21 was utilized. FITC-labeled Aim21 peptides FITC-KIEFNNWNVS (FITC-Aim21), FITC-KIEAANNWNVS (FITC-Aim21\*), and FITC-KTGPLGGTRRGRGPRGRKLPKVASVEKIEEDNTNKIEIFNNWNVS (FITC-Aim21<sup>CPH+TBR</sup>) were purchased from Thermo Fisher, Biomatik, and GenScript, respectively. Data were collected using 384-well nonbinding polystyrene microplates (Greiner Bio-one) in a Victor<sup>3</sup> V microplate reader (PerkinElmer) at room temperature following a 30-min incubation. Three technical replicates were performed per experiment and each experiment was performed three independent times. The dissociation constants for each independent experiment were determined by curve fitting the data to either one-site or two-site binding isotherms using GraphPad Prism Software. The reported dissociation constants correspond to the average (and SEM) of values obtained in the three independent experiments.

Total yeast extracts were obtained as previously described (Di Pietro *et al.*, 2010). Immunoblotting of cell extract was performed using anti-GFP (Sigma). For Aim21-GFP immunoblotting, transfer buffer was supplemented with 0.1% SDS for increased transfer efficiency of Aim21-GFP.

Size-exclusion chromatography for analysis of Tda2 and Tda2 mutants was performed on a Superdex 75 Increase 10/300 GL column (GE Healthcare) connected to a fast protein liquid chromatography system (GE Healthcare). The column was equilibrated with PBS at 4°C, and elution of 0.5 mg/ml protein sample was performed at a flow rate of 0.5 ml/min. Size-exclusion chromatography for analysis of the Tda2-Aim21 Complex was performed on a Superose 6 10/300 GL column (GE Healthcare) connected to a fast protein liquid chromatography system (GE Healthcare). The column was equilibrated with PBS at 4°C, and elution was performed at a flow rate of 0.4 ml/min with fractions collected every 750 μl. His-Aim21 was used at a concentration of 0.5 mg/ml, and His-Tda2 was matched at an equimolar concentration. Fractions were mixed with Laemmli sample buffer and analyzed by SDS. The column was calibrated using blue dextran and a set of standard protein of known Stokes radii: cytochrome *c* (17 Å, 12 kDa), carbonic anhydrase (21 Å, 29 kDa), bovine serum albumin (BSA; 35 Å, 66 kDa), alcohol dehydrogenase (46 Å, 150 kDa), apoferritin (61 Å, 443 kDa), and thyroglobulin (86 Å, 669 kDa). A standard curve was used for estimation of experimental Stokes radii.

Sucrose density linear gradients (5–20% wt/vol) were formed using a Gradient Master (BioComp); 200 μl of protein sample was layered on top of the gradient, and the samples were centrifuged in a SW 41 Ti rotor (Beckman Coulter) at 39,000 RPM for 18 h at 4°C. Then, 500 μl fractions were collected from the top of the test tube using a Piston Gradient Fractionator (BioComp Instruments). Fractions were analyzed by SDS-PAGE and Coomassie staining.

A set of standard proteins of known *S* were analyzed for comparison: cytochrome *c* (1.5 *S*, 12kDa), ovalbumin (3.6 *S*, 43 kDa), BSA (4.6 *S*, 66 kDa), and bovine catalase (11.3 *S*, 250 kDa). A standard curve was used for estimation of experimental *S*.

## Fluorescence Microscopy

Fluorescence microscopy was performed as previously described using an IX81 spinning-disk confocal microscope (Olympus) with a Cascade II camera (Photometrics) and a 100× 1.40 NA objective (Tolsma *et al.*, 2018). Briefly, cells grown overnight were diluted in synthetic complete media and grown to early logarithmic phase, then imaged at room temperature. Time-lapse videos were generated by collecting an image each second for 90 s. Slidebook 6 software (Intelligent Imaging Innovations) was used for quantification of patch intensities and lifetimes. For Cap1-GFP, Abp1-GFP, and

Abp1-mCherry analysis, time-lapse videos were used for quantification of peak patch intensities and patch lifetimes. To avoid issues with photobleaching, Aim21-GFP analysis of patches was done using still images. For quantification of peak patch/cytosol ratios, masks were drawn over individual endocytic sites to track the average fluorescence of the patch over time. Average patch intensity, average cytosol intensity, and average background intensity were recorded for the frame in which the average patch intensity was at its maximum. After subtracting the average background from both values, the values were divided to give the peak patch/cytosol ratio. For quantification of patch lifetimes, masks were drawn over individual endocytic patches to track the maximum fluorescence of each patch over time. Prior to quantification, a threshold fluorescence value was established for each fluorescently tagged protein to establish a start and finish value for the endocytic event. The patch lifetime was determined by counting the number of frames in which the maximum patch fluorescence was above the threshold value. Patch/cytosol ratios were calculated in the same manner as peak/patch cytosol ratios, but using still images. Statistical significance between groups was determined using a Mann–Whitney test for all microscopy data (GraphPad Prism Software). Representative images for groups that were directly compared were displayed with equal brightness and contrast settings.

The B/B homodimerizer AP20187 (Takara Bio) was utilized in a similar manner as described previously. Briefly, cells were grown overnight in synthetic complete media. The following day, cells were diluted into fresh synthetic complete media and grown to early log phase. 90 min/Ninety minutes prior to imaging, 5  $\mu$ M AP20187 or an equal volume of EtOH was added to the cultures, and cells were imaged as described.

## ACKNOWLEDGMENTS

The microscope used in this work is supported in part by the CSU Microscope Imaging Network core infrastructure grant. This work was supported by NSF Grant MCB-1616775 and National Institutes of Health Grant GM-125619 to S.D.P.

## REFERENCES

- Amatruda JF, Cannon JF, Tatchell K, Hug C, Cooper JA (1990). Disruption of the actin cytoskeleton in yeast capping protein mutants. *Nature* 344, 352–354.
- Avinoam O, Schorb M, Beese CJ, Briggs JA, Kaksonen M (2015). ENDOCYTOSIS. Endocytic sites mature by continuous bending and remodeling of the clathrin coat. *Science* 348, 1369–1372.
- Benison G, Barbar E (2009). NMR analysis of dynein light chain dimerization and interactions with diverse ligands. *Methods Enzymol* 455, 237–258.
- Boettner DR, Chi RJ, Lemmon SK (2012). Lessons from yeast for clathrin-mediated endocytosis. *Nat Cell Biol* 14, 2–10.
- Bruck S, Huber TB, Ingham RJ, Kim K, Niederstrasser H, Allen PM, Pawson T, Cooper JA, Shaw AS (2006). Identification of a novel inhibitory actin-capping protein binding motif in CD2-associated protein. *J Biol Chem* 281, 19196–19203.
- Bultema JJ, Boyle JA, Malenke PB, Martin FE, Dell'Angelica EC, Cheney RE, Di Pietro SM (2014). Myosin vc interacts with Rab32 and Rab38 proteins and works in the biogenesis and secretion of melanosomes. *J Biol Chem* 289, 33513–33528.
- Burston HE, Maldonado-Baez L, Davey M, Montpetit B, Schluter C, Wendland B, Conibear E (2009). Regulators of yeast endocytosis identified by systematic quantitative analysis. *J Cell Biol* 185, 1097–1110.
- Chuang JZ, Yeh TY, Bollati F, Conde C, Canavosio F, Caceres A, Sung CH (2005). The dynein light chain Tctex-1 has a dynein-independent role in actin remodeling during neurite outgrowth. *Dev Cell* 9, 75–86.
- Clackson T, Yang W, Rozamus LW, Hatada M, Amara JF, Rollins CT, Stevenson LF, Magari SR, Wood SA, Courage NL, et al. (1998). Redesigning an FKBP-ligand interface to generate chemical dimerizers with novel specificity. *Proc Natl Acad Sci USA* 95, 10437–10442.
- Clark SA, Jespersen N, Woodward C, Barbar E (2015). Multivalent IDP assemblies: Unique properties of LC8-associated, IDP duplex scaffolds. *FEBS Lett* 589, 2543–2551.
- Conde C, Arias C, Robin M, Li A, Saito M, Chuang JZ, Nairn AC, Sung CH, Caceres A (2010). Evidence for the involvement of Lfc and Tctex-1 in axon formation. *J Neurosci* 30, 6793–6800.
- Di Pietro SM, Cascio D, Feliciano D, Bowie JU, Payne GS (2010). Regulation of clathrin adaptor function in endocytosis: novel role for the SAM domain. *EMBO J* 29, 1033–1044.
- Doyon JB, Zeitler B, Cheng J, Cheng AT, Cherone JM, Santiago Y, Lee AH, Vo TD, Doyon Y, Miller JC, et al. (2011). Rapid and efficient clathrin-mediated endocytosis revealed in genome-edited mammalian cells. *Nat Cell Biol* 13, 331–337.
- Edwards M, Liang Y, Kim T, Cooper JA (2013). Physiological role of the interaction between CARMIL1 and capping protein. *Mol Biol Cell* 24, 3047–3055.
- Edwards M, McConnell P, Schafer DA, Cooper JA (2015). CPI motif interaction is necessary for capping protein function in cells. *Nat Commun* 6, 8415.
- Edwards M, Zwolak A, Schafer DA, Sept D, Dominguez R, Cooper JA (2014). Capping protein regulators fine-tune actin assembly dynamics. *Nat Rev Mol Cell Biol* 15, 677–689.
- Falck S, Paavilainen VO, Wear MA, Grossmann JG, Cooper JA, Lappalainen P (2004). Biological role and structural mechanism of twinfilin-capping protein interaction. *EMBO J* 23, 3010–3019.
- Farrell KB, Grossman C, Di Pietro SM (2015). New regulators of clathrin-mediated endocytosis identified in *Saccharomyces cerevisiae* by systematic quantitative fluorescence microscopy. *Genetics* 201, 1061–1070.
- Farrell KB, McDonald S, Lamb AK, Worcester C, Peersen OB, Di Pietro SM (2017). Novel function of a dynein light chain in actin assembly during clathrin-mediated endocytosis. *J Cell Biol* 216, 2565–2580.
- Feliciano D, Di Pietro SM (2012). SLAC, a complex between Sla1 and Las17, regulates actin polymerization during clathrin-mediated endocytosis. *Mol Biol Cell* 23, 4256–4272.
- Feliciano D, Tolsma TO, Farrell KB, Aradi A, Di Pietro SM (2015). A second Las17 monomeric actin-binding motif functions in Arp2/3-dependent actin polymerization during endocytosis. *Traffic* 16, 379–397.
- Fujiwara I, Remmert K, Piszczek G, Hammer JA (2014). Capping protein regulatory cycle driven by CARMIL and V-1 may promote actin network assembly at protruding edges. *Proc Natl Acad Sci USA* 111, E1970–E1979.
- Goode BL, Eskin JA, Wendland B (2015). Actin and endocytosis in budding yeast. *Genetics* 199, 315–358.
- Hakala M, Wioland H, Tolonen M, Kotila T, Jegou A, Romet-Lemonne G, Lappalainen P (in press). Twinfilin uncaps filament barbed ends to promote turnover of lamellipodial actin networks. *Nat Cell Biol*.
- Hakala M, Wioland H, Tolonen M, Kotila T, Jegou A, Romet-Lemonne G, Lappalainen P (2021). Twinfilin uncaps filament barbed ends to promote turnover of lamellipodial actin networks. *Nat Cell Biol* 23, 147–159.
- Hall J, Karplus PA, Barbar E (2009). Multivalency in the assembly of intrinsically disordered Dynein intermediate chain. *J Biol Chem* 284, 33115–33121.
- Hernandez-Valladares M, Kim T, Kannan B, Tung A, Aguda AH, Larsson M, Cooper JA, Robinson RC (2010). Structural characterization of a capping protein interaction motif defines a family of actin filament regulators. *Nat Struct Mol Biol* 17, 497–503.
- Hess DC, Myers CL, Huttenhower C, Hibbs MA, Hayes AP, Paw J, Clore JJ, Mendoza RM, Luis BS, Nislow C, et al. (2009). Computationally driven, quantitative experiments discover genes required for mitochondrial biogenesis. *PLoS Genet* 5, e1000407.
- Huh WK, Falvo JV, Gerke LC, Carroll AS, Howson RW, Weissman JS, O'Shea EK (2003). Global analysis of protein localization in budding yeast. *Nature* 425, 686–691.
- Idrissi FZ, Blasco A, Espinal A, Geli MI (2012). Ultrastructural dynamics of proteins involved in endocytic budding. *Proc Natl Acad Sci USA* 109, E2587–E2594.
- Iserberg G, Aebi U, Pollard TD (1980). An actin-binding protein from *Acanthamoeba* regulates actin filament polymerization and interactions. *Nature* 288, 455–459.
- Ito H, Fukuda Y, Murata K, Kimura A (1983). Transformation of intact yeast cells treated with alkali cations. *J Bacteriol* 153, 163–168.
- Jespersen N, Barbar E (2020). Emerging features of linear motif-binding hub proteins: (Trends in Biochemical Sciences, 45, 375–384, 2020). *Trends Biochem Sci* 4, 921.
- Johnson B, McConnell P, Kozlov AG, Mekel M, Lohman TM, Gross ML, Amarasinghe GK, Cooper JA (2018). Allosteric coupling of CARMIL

- and V-1 binding to capping protein revealed by hydrogen-deuterium exchange. *Cell Rep* 23, 2795–2804.
- Johnston AB, Hilton DM, McConnell P, Johnson B, Harris MT, Simone A, Amarasinghe GK, Cooper JA, Goode BL (2018). A novel mode of capping protein-regulation by twinfilin. *Elife* 7.
- Kaksonen M, Toret CP, Drubin DG (2005). A modular design for the clathrin- and actin-mediated endocytosis machinery. *Cell* 123, 305–320.
- Kim K, Yamashita A, Wear MA, Maeda Y, Cooper JA (2004). Capping protein binding to actin in yeast: biochemical mechanism and physiological relevance. *J Cell Biol* 164, 567–580.
- Kolos JM, Voll AM, Bauder M, Hausch F (2018). FKBP ligands—Where we are and where to go? *Front Pharmacol* 9, 1425.
- Kukulski W, Schorb M, Kaksonen M, Briggs JA (2012). Plasma membrane reshaping during endocytosis is revealed by time-resolved electron tomography. *Cell* 150, 508–520.
- McMahon HT, Boucrot E (2011). Molecular mechanism and physiological functions of clathrin-mediated endocytosis. *Nat Rev Mol Cell Biol* 12, 517–533.
- Merino-Gracia J, Garcia-Mayoral MF, Rapali P, Valero RA, Bruix M, Rodriguez-Crespo I (2015). DYNLT (Tctex-1) forms a tripartite complex with dynein intermediate chain and RagA, hence linking this small GTPase to the dynein motor. *FEBS J* 282, 3945–3958.
- Merrifield CJ, Feldman ME, Wan L, Almers W (2002). Imaging actin and dynamin recruitment during invagination of single clathrin-coated pits. *Nat Cell Biol* 4, 691–698.
- Mionnet C, Bogliolo S, Arkowitz RA (2008). Oligomerization regulates the localization of Cdc24, the Cdc42 activator in *Saccharomyces cerevisiae*. *J Biol Chem* 283, 17515–17530.
- Mooren OL, Galletta BJ, Cooper JA (2012). Roles for actin assembly in endocytosis. *Annu Rev Biochem* 81, 661–686.
- Mwangangi DM, Manser E, Robinson RC (2021). The structure of the actin filament uncapping complex mediated by twinfilin. *Sci Adv* 7.
- Neff T, Blau CA (2001). Pharmacologically regulated cell therapy. *Blood* 97, 2535–2540.
- Newpher TM, Smith RP, Lemmon V, Lemmon SK (2005). In vivo dynamics of clathrin and its adaptor-dependent recruitment to the actin-based endocytic machinery in yeast. *Dev Cell* 9, 87–98.
- Palmgren S, Ojala PJ, Wear MA, Cooper JA, Lappalainen P (2001). Interactions with PIP2, ADP-actin monomers, and capping protein regulate the activity and localization of yeast twinfilin. *J Cell Biol* 155, 251–260.
- Rapali P, Szenes A, Radnai L, Bakos A, Pal G, Nyitray L (2011). DYNLL/LC8: a light chain subunit of the dynein motor complex and beyond. *FEBS J* 278:2980–2996.
- Reider A, Wendland B (2011). Endocytic adaptors-social networking at the plasma membrane. *J Cell Sci* 124, 1613–1622.
- Shekhar S, Hoeprich GJ, Gelles J, Goode BL (2021). Twinfilin bypasses assembly conditions and actin filament aging to drive barbed end depolymerization. *J Cell Biol* 220.
- Shin M, van Leeuwen J, Boone C, Bretscher A (2018). Yeast Aim21/Tda2 both regulates free actin by reducing barbed end assembly and forms a complex with Cap1/Cap2 to balance actin assembly between patches and cables. *Mol Biol Cell* 29, 923–936.
- Sikorski RS, Hieter P (1989). A system of shuttle vectors and yeast host strains designed for efficient manipulation of DNA in *Saccharomyces cerevisiae*. *Genetics* 122, 19–27.
- Stark BC, Lanier MH, Cooper JA (2017). CARMIL family proteins as multidomain regulators of actin-based motility. *Mol Biol Cell* 28, 1713–1723.
- Taylor MJ, Perrais D, Merrifield CJ (2011). A high precision survey of the molecular dynamics of mammalian clathrin-mediated endocytosis. *PLoS Biol* 9, e1000604.
- Tolsma TO, Cuevas LM, Di Pietro SM (2018). The Sla1 adaptor-clathrin interaction regulates coat formation and progression of endocytosis. *Traffic* 19, 446–462.
- Weinberg J, Drubin DG (2012). Clathrin-mediated endocytosis in budding yeast. *Trends Cell Biol* 22, 1–13.
- Williams JC, Roulhac PL, Roy AG, Vallee RB, Fitzgerald MC, Hendrickson WA (2007). Structural and thermodynamic characterization of a cytoplasmic dynein light chain-intermediate chain complex. *Proc Natl Acad Sci USA* 104, 10028–10033.
- Williams JC, Xie H, Hendrickson WA (2005). Crystal structure of dynein light chain TcTex-1. *J Biol Chem* 280, 21981–21986.
- Yeh TY, Peretti D, Chuang JZ, Rodriguez-Boulan E, Sung CH (2006). Regulatory dissociation of Tctex-1 light chain from dynein complex is essential for the apical delivery of rhodopsin. *Traffic* 7, 1495–1502.